LUND UNIVERSITY

Master Thesis

Mathematical Modeling and Simulation of Cryogenic Liquid Hydrogen Storage

— A contribution to Modelon's component libraries —

by

Gusten Zandler Andersson

Department of Chemical Engineering
Lund University
Sweden
May 25, 2023

Company Supervisor: **Daniel Andersson, Modelon AB**
University Supervisor: **Doctor Niklas Andersson**
Examiner: **Professor Bernt Nilsson**

Postal address	**Visiting address**	**Telephone**
PO-Box 124	Naturvetarvägen 14	+46 46-222 82 85
SE-221 00 Lund, Sweden		+46 46-222 00 00

Web address
www.lth.se/chemeng

© 2023 by Gusten Zandler Andersson. All rights reserved.
Printed in Sweden by Media-Tryck.
Lund 2023

Acknowledgement

I want to start by thanking Modelon for offering me the opportunity to write my master's thesis at their company, and for providing me with all the necessary resources and support. I would like to thank my company supervisors Daniel Andersson and Clement Coïc for the all the help and valuable insight they have provided me throughout the course of the project, and for the tremendous patience they've displayed with me. Additionally I would like to thank my university supervisor Niklas Andersson for the many insightful discussions and suggestions regarding the many problems encountered during the making of this thesis.

Lastly, I would like to express my gratitude to my family for supporting me all throughout my academic career and for believing in me. I want to give special thanks to my wonderful wife who has been my main source of inspiration and given me the motivation to work hard and always try my best.

Thank You!

Abstract

Liquid hydrogen is an attractive alternative to fossil fuels in the aviation industry, but storing it both before and during flights introduces many challenges pertaining to the cryogenic liquid conditions required. Having reliable models to predict the dynamical behavior inside the storage tank is therefore of great interest.

This thesis covers the development of a low-dimensional model for a liquid hydrogen storage tank capable of describing boil-off and self-pressurization dynamics by taking into account thermal stratification effects brought on by natural convection. The model uses experimentally derived correlations to estimate the flow characteristics and heat transfer of the liquid domain by dividing it into several horizontal control volumes. Additionally it tries to incorporate highly non-equilibrium descriptions of the evaporation/condensation phenomena at the interface and a non-conventional discretization approach to solve for the temperature profile close to said interface is suggested.

Validation showed that the model can produce results closely matching experimental self-pressurization data when calibrated parameters are employed, but not necessarily for all experimental setups. Furthermore, the model was successfully utilized to simulate several common storage scenarios and generate data for analysis. Recurring issues with model robustness encumbers the flexibility and usefulness of the model, and as such more work is required on its development.

Sammanfattning

Flytande väte är på väg att bli ett alternativ till mer traditionalla fossilbaserade drivmedel inom flygindustrin, men förvaring av vätskan kan innebära en stor utmaning på grund av cryogeniska förhållanden. Av denna anldedning finns det ett stort intresse för pålitliga simuleringsmodeller som kan reproducera de dynamiska processer som äger rum inuti förvaringstanken.

Detta examensarbete beskriver utveklingen av en lågdimensionell model för en förvaringstank med flytande väte med förmågan att beskriva dynamiken bakom förångings-och självtrycksfenomen som uppstår under förvaring genom att ta hänsyn till termiska skiktningseffecter orsakade av naturlig konvektion. Modellen använder experimentellt framtagna korrelationer för att uppskatta flödeskaraktär och värmetransport i vätskefasen genom att fördela tanken i flera horisontella kontrollvolymer. Modellen innehåller icke-jämviktsbeskrivingar av förångnings-och kondenseringsfenomen vid gränsnittet mellan gas-och vätske fas. Ett okonventionellt tillvägagångsätt för att lösa temperaturprofilen nära gränssnittet via diskretisering är också presenterat.

Modellvalidering visar att modelen är kapabel att producera simuleringsresultat med bra likhet till experimentela värden när kalibrerade parametrar används, men att detta inte nödvändigtvis är fallet för alla experimentella uppställningar. Modellen kunde frangångsrikt användas för att simulera flera vanliga förvaringssenarior och generera data för vidare analys. Återkommande problem med robusthet och stabilitet leder till begränsad flexibilitet och generell användbarhet av modellen, och mer arbete med dess utvekling är därför nödvändigt.

Popular science summary

Transitioning away from fossil fuels is an important step in the ongoing battle to minimize global effects of greenhouse gas emissions. Liquid hydrogen is believed to one day play a key role in this transitioning process, especially as a potential alternative fuel source for air travel. A problem with liquid hydrogen is that storing it, either on the ground or onboard an aircraft, comes with many new challenges due to the extreme temperature conditions and resulting processes happening inside the storage tank. It is therefore of great interest that there exists models that can be used to predict these processes.

This thesis work presents the creation of a model that is able to simulate the inner dynamics of a liquid hydrogen storage tank. With the help of well established theory, mathematical modeling and experimental observations the model can be used to describe pressure and temperature change in a tank as it is exposed to environmental conditions. It also introduces an interesting suggestion on how to model evaporation and condensation of the hydrogen.

The model can reproduce pressure and temperature results similar to those seen in experimental studies of liquid hydrogen storage when certain predefined parameters are used. Additionally, the model was used successfully to simulate a number of different storage scenarios that are of general interest. Unfortunately, because of fundamental modeling issues the current version of the model is limited in terms of flexibility and usefulness, and more work to improve the model is still required.

Populärvetenskaplig sammanfattning

Att övergå från fossila bränslen är ett viktigt steg i den pågående kampen för att minimera globala effekter av växthusgaser. Flytande väte tros en dag spela en nyckelroll i denna övergångsprocess, särskilt som ett potentiellt alternativt bränsle inom flygindustrin. Ett problem med flytande väte är att dess förvaring, antingen på marken eller ombord på ett flygplan, introducerar många nya utmaningar. Detta är på grund av de extremt kalla temperaturer och resulterande i processer som sker inuti lagringstanken. Det är därför av stort intresse att utveckla modeller som kan användas för att förutsäga dessa processer.

Detta examensarbete presenterar en modell som kan simulera den inre dynamiken i en lagringstank för flytande väte. Med hjälp av väletablerad teori, matematisk modellering och experimentella observationer kan modellen användas för att beskriva tryck- och temperaturförändringar i en tank när den utsätts för påverkan från omgivningen. Den introducerar också ett intressant förslag på hur man kan modellera avdunstning och kondensation av väte.

Modellen kan producera tryck- och temperaturresultat som liknar de från experimentella studier av lagring med flytande väte när fördefinierade parametrar är givna. Dessutom användes modellen framgångsrikt för att simulera ett antal olika lagringsscenarier som är av allmänt intresse. På grund av fundamentala modelleringsproblem är den nuvarande versionen av modellen tyvärr begränsad vad gäller flexibilitet och användbarhet, och mer arbete krävs för att förbättra den innan den kan användas rent generellt.

Contents

1 Introduction

1.1 Overview

Hydrogen is considered to be a promising alternative to traditional fossil fuels, as its clean-burning properties makes it a desirable energy source for propulsion systems and power generation. In case of the latter, hydrogen can also be used in a fuel cell to generate electricity to power e.g., a flight propeller. The main challenge with using hydrogen as a fuel at ambient conditions is its gaseous state, which results in low energy densities and the need for often impractically large storage volumes. One proposed strategy of achieving sufficient energy density for e.g aeronautic applications is to store liquid hydrogen at cryogenic temperatures (around 20 K), which would circumvent the need for energy demanding gas compression prior to and during storage [1].

Due to the inherent difference in temperature between stored liquid hydrogen and ambient conditions, heat ingress into the storage tank is unavoidable even when high-end thermal insulation is used. This leads to evaporation of the contained liquid, which in turn increases the pressure inside the storage tank. To design a tank for optimal storage of liquid hydrogen for the time scale required, having accurate models to predict and control pressure rise is paramount [2].

Modelon currently has an existing model in their ThermoFluid library that can be used to simulate the pressure evolution over time inside of a cryogenic hydrogen storage tank. However, the simulated pressure change does not fully match experimental results [3]. It is believed that this is due to certain physical phenomena occurring during the real process not being included in the existing model, which at the moment is a rather simplified representation of a general two-phase system.

1.2 Aim

The aim of this thesis is to contribute to the development of a liquid hydrogen storage tank model that is capable of better describing the underlying dynamics inside of the tank. This is to be done using the object-oriented, equation-based modeling language Modelica. The goal is for the model to have suitable fidelity for integration in large system models, for example a complete aircraft driveline, which means that the time needed for simulation should be kept relatively short. As such, comprehensive 3D computational fluid dynamic (CFD) modeling approaches should be avoided.

2 Background

2.1 Theory

2.1.1 Liquid Hydrogen

As mentioned briefly in the introduction, hydrogen possesses several advantages as a fuel source when compared to other alternatives currently in use. Its wide flammability range (4-74% concentration in air) makes it quite suitable for combustion engines since it results in good fuel economy and generally low combustion temperatures. The latter also reduces the amount of potential pollutants emitted from the exhaust. The high auto-ignition temperature of hydrogen also enables higher compression ratios within the engine, which gives rise to an overall greater thermal efficiency when compared to a conventional hydrocarbon engine [4]. One of its biggest allures is the fact that when burnt, hydrogen produces no carbon emissions. This means that as long as the production of hydrogen was done via renewable means it is possible to have a fuel that emits net zero CO2 [5].

On the basis of mass, hydrogen also contains tree times more energy than conventional jet fuel and over a hundred times more than a traditional lithium-ion battery, which makes it particularly well suited for aviation applications. The main challenge is the very poor energy density per unit volume, which results in the need for almost 3000 liters of hydrogen-gas for every liter of kerosene to achieve the same amount of energy [6]. One way to improve this is to compress the gas at around 700 bars of pressure, as is often done with hydrogen powered automobiles, however this is not desirable for all applications [1]. Instead, the highest energy densities are obtained when hydrogen is in its liquid form, which occurs when it is cooled to a temperature below -253 °C (or roughly 20K) at atmospheric pressure. Storing liquid hydrogen – both prior to and during flights – introduces new challenges; a large one being heat transfer from the environment into the storage tank.

2.1.2 Boil-off rate and self-pressurization

As heat leaks into the cryogenic liquid storage vessel, some amount of hydrogen will transition from the liquid phase and evaporate away as what is commonly referred to as boil-of gas (BOG) into the ullage part of the tank. The generation of BOG inevitably leads to a phenomenon known as self-pressurization, in which the pressure within the storage vessel can slowly increase to the point of venting being required [7]. Venting of BOG will, after a long enough period, of course entail an effective loss of valuable fuel. The rate at which BOG production occurs is dependent on factors such as insulation material (thickness and quality) as well as storage tank geometry and proportion (i.e., surface-to-volume ratio and filling level). In the case of liquid hydrogen it has been reported that boil-of rates for 50 m^3 storage tanks can be upwards of 7 times higher in terms of percent liquid-loss per day when compared to a 20 000 m^3 tank [8]. Experiments done by Hasan et al. have also showed that the rate of self-pressurization at the early stage of non-vented storage depends significantly on the initial storage condition used (see Figure 2.1) [3]. In the case of an *isothermal* starting condition — i.e., when all vent valves are closed immediately after filling the tank — a rapid initial pressure rise is observed. In contrast, if the boil-off rate and tank wall temperatures are allowed to stabilize before closing the vent, a *steady boil-off* starting condition is achieved and the initial pressure rise is less pronounced.

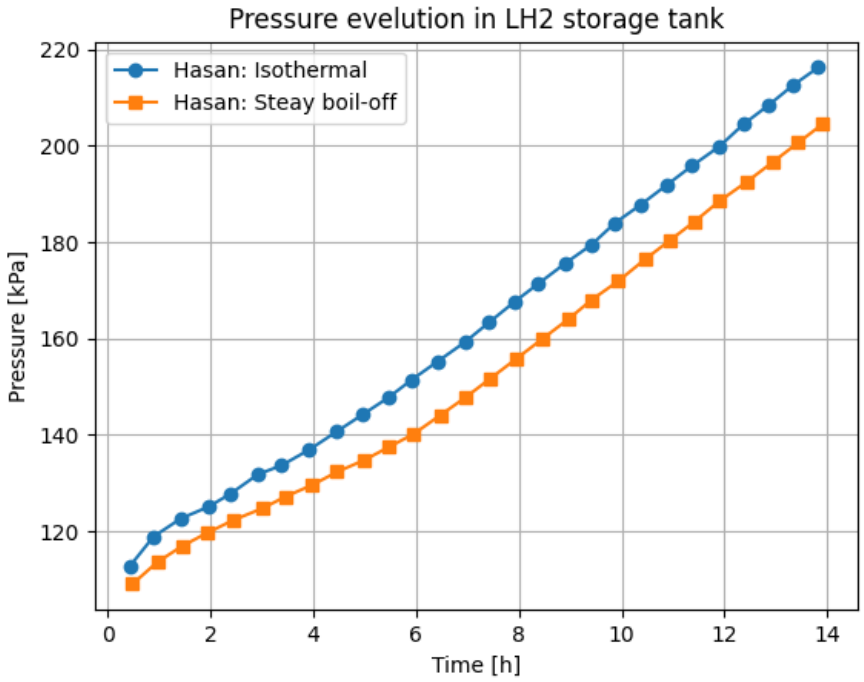

Figure 2.1 – Experimentally observed pressure rise for two different starting conditions inside a spherical liquid hydrogen storage tank.

2.1.3 Thermal stratification

It is well established that the main contributing factor behind increased pressure evolution rates is the formation of a thermal stratification layer within the liquid domain of the storage tank. At normal gravity conditions, wall heating generally contributes the most to the formation of thermal stratification as liquid in contact with the wetted tank walls experiences convective movement vertically alongside the wall towards the liquid surface brought on by buoyancy forces. This naturally leads to a growing stratified liquid layer at the interface that has a higher temperature than the remaining bulk liquid volume. As hot liquid exchanges heat and mass at the interface it becomes more dense and sinks back to the liquid bulk. A schematic depiction of this convective flow can be seen in Figure 2.2. Since the boil-off rate dependent on the liquid-gas interface temperature, this non-homogeneous temperature distribution gives rise to a greater pressure evolution rate compared to if the cryogenic liquid had been thermally uniform [3, 7–9].

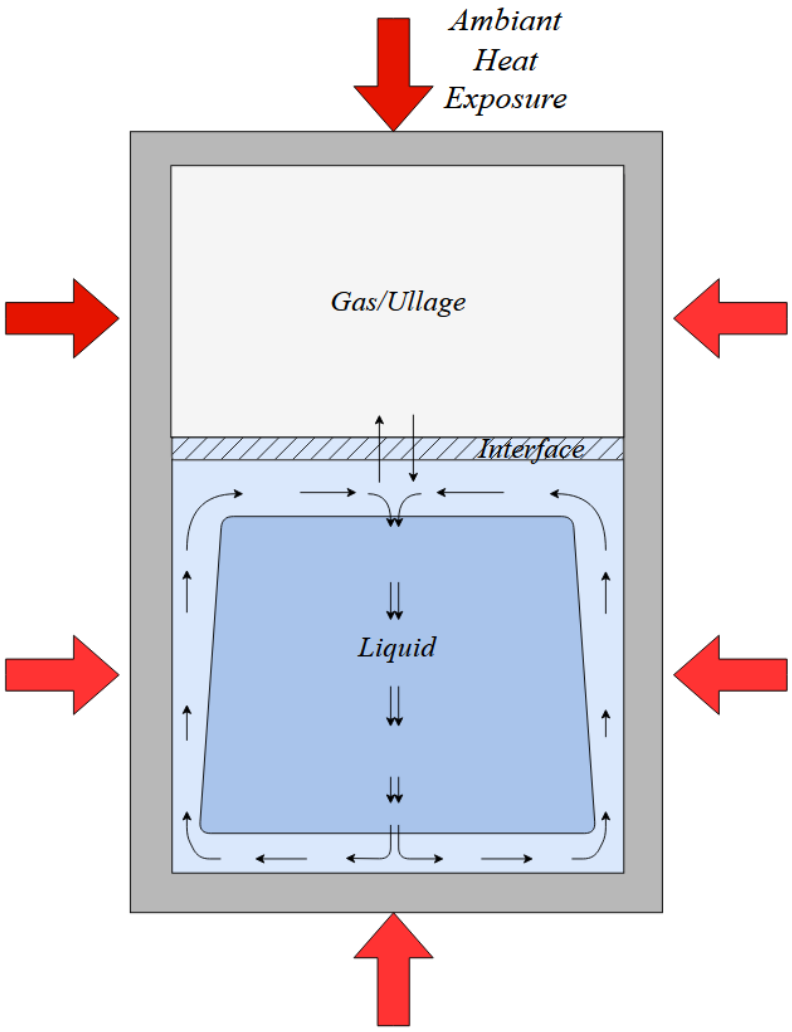

Figure 2.2 – Buildup of thermal stratification layer within the liquid phase over time as heat is transferred across the wall into the storage tank. The thermal stratification layer is depicted in light blue in the Figure.

2.2 Literature study

Since thermal stratification seems to be a main factor dictating the dynamics of the tank, investigating and evaluating different ways of describing this phenomenon is of great relevance for the goal of this thesis.

There have been numerous articles written on the topic of cryogenic storage of hydrogen and subsequent model development to represent the associated phenomena. Al Ghafri et al. [**1**] developed a simple non-CFD model using a non-equilibrium approach in the software package BoilFAST for calculation of self-pressurization

and boil-off losses for liquid hydrogen that produced results in good agreement with experimental data. Although being flexible in regards to spin isomer composition in each phase, the model did not take thermal stratification into account. Liu et al. [10] introduced a CFD based model created in the simulation software FLUENT 14.0 and found that the obtained thermal stratification layer thickness and temperature profile were similar to those predicted by theoretical models. Joseph and Agrawal et al. [11] developed a multi-phase thermodynamic model of a foam insulated LH2 tank to study the effects of insulation thickness on pressure evolution and liquid stratification using the fluid flow design software SINDA/FLUINT. The model was validated with transient pressure and temperature data from experiments found in literature, and the authors concluded that tank pressure, which is tied to the liquid/vapor interface temperature, has a significant effect on the stratified mass evolution. Daigle et al. [12] presented a reduced dynamical model for describing temperature stratification effects driven by natural convection in a LH2 fuel tank by dividing the tank into multiple horizontal control volumes for both the liquid and vapor space domains. Temperature and velocity boundary layers close to the tank wall were introduced using established correlations, and non-equilibrium condensation-evaporation phenomena at the interface were also included. It was concluded that complex thermodynamic processes could be accurately portrayed by means of a simplified computational approach (mainly not involving full-on CFD methodology). Similarly, Gursu et al. [13] developed three low-dimensional pressure rise models: two homogeneous temperature models and one thermal stratification model; to calculate the self-pressurization and boil-off rate in cryogenic liquid vessels. It was found that only the thermal stratification model could produce results consistent with experimental observations, and they too concluded that thermal stratification is one of the primary factors when determining pressure rise rate. Other examples of simple modeling approaches showing reasonable fidelity when validated with experimental data can be found in [14–16]. Additionally, there have been many models developed to predict pressure evolution and stratification phenomena during storage of cryogenic liquids other than hydrogen [17–20].

The issue with many of the models already developed is that they either rely on commercially available fluid dynamics software with very complex systems, or make fairly large assumptions when describing the phenomena of interest. Creating a model that is able to describe the more complex dynamics of a hydrogen storage

system without itself being overly complicated would be a welcomed contribution to Modelon's component libraries.

2.3 Modelon and Modelica

Modelon is a multinational software company that specializes in providing software solutions and expert services to different organizations in need of model-based simulation tools for design and development of technical systems. Their leading products include libraries, solvers and development solutions for modeling, simulation and optimization. The model presented in this thesis was created using Modelon Impact, Modelons flagship product. Impact is a cloud based systems simulation platform developed to assist engineers to visually design, analyse and simulate a large variety of physical systems. For more information abound Modelon and Modelon Impact, please visit `https://modelon.com/company/` [21].

All modeling was implemented using the object-oriented, equation-based modeling language Modelica. The language emphasises mathematical modeling of the dynamical behavior of technical systems consisting of components from several different domains in a convenient way. A Modelica class, in this context more often referred to as a class model or simulation model, can be described using differential, algebraic and discrete equations that are transformed into a flat Modelica structure called a flat hybrid DAE. Specific semantic restrictions exists for a simulation model to ensure that the model is complete, however, the Modelica specification does not dictate how the model is simulated. Instead, it is up to the simulation engine to manipulate all equations symbolically to determine the order of their execution [22].

3 Modeling Methodology

3.1 Tank model

The following model is based in part on the design described by Daigle et al. [12], as this approach provides a relatively simple way of representing the temperature distribution throughout the tank without the need of very fine mesh generation or intricate flow-field calculations. A vertically oriented cylindrical tank with flat ends will be used to illustrate and derive the various equations and correlations underlying the mathematical modelling, however, other common geometries will be considered later on in the report.

3.1.1 Thermal stratification model

The liquid domain of the storage tank is divided into several horizontal control volumes with equal heights (see Figure 3.1). As a consequence, the height of any one control volume h_i can be easily defined as the ratio between the liquid level in the tank at a given time and the number of horizontal layers in the liquid domain:

$$h_i = \frac{h_{level}}{n} \tag{3.1}$$

Here, h_{level} will be a function of the liquid volume in conjunction with the geometric features of the tank, as will be addressed later. n is an integer parameter chosen by the user.

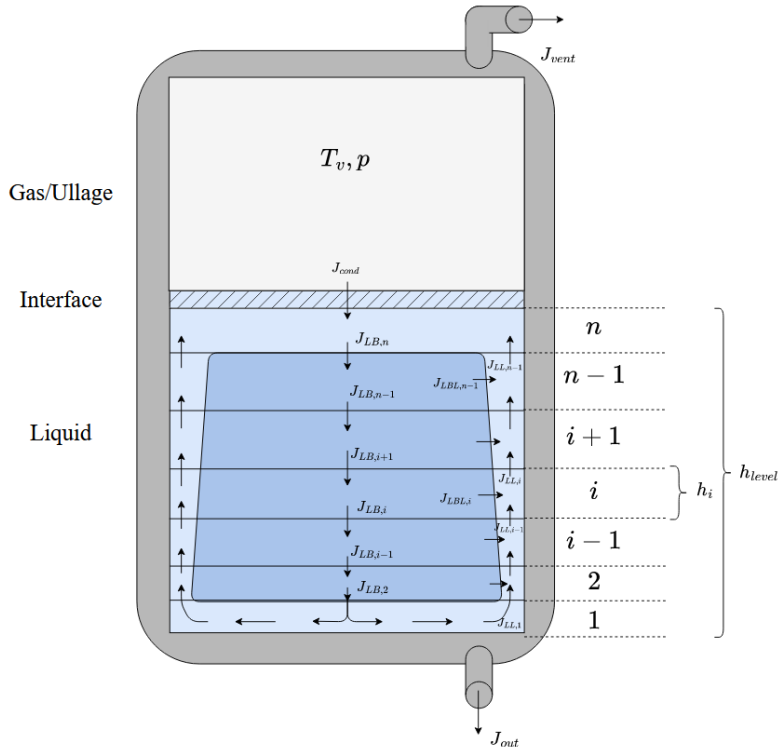

Figure 3.1 – Division of liquid domain into n horizontal control volumes. The direction of different mass flows J are represented by the arrows.

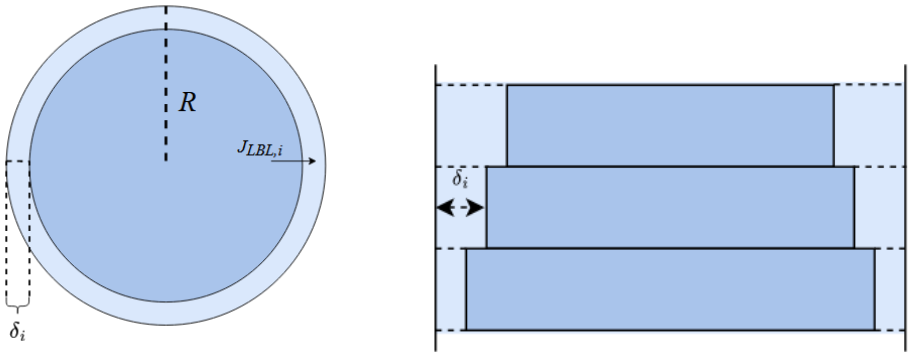

(a) Top-down view (Horizontal slice).

(b) Side view.

Figure 3.2 – Horizontal slice of liquid domain showing division of liquid bulk and boundary layer in a vertically oriented cylindrical tank with radius R.

Each horizontal liquid slice is further divided into two sub-domains: The *liquid bulk*, denoted LB, which contains the majority of fluid kept relatively uniform; and the *liquid/lateral boundary layer*, denoted LL, which describes the hotter layer subjected

to upwards vertical flow in contact with the tank wall. It is here assumed that there is no boundary layer formation in the first and last control volumes ($i = 1$ and $i = n$). The total volume of the liquid domain will be the sum of all individual LB and LL control volume contributions:

$$V_{liq} = \sum_{i=2}^{n-1} (V_{LB,i} + V_{LL,i}) + V_{LB,1} + V_{LB,n} \tag{3.2}$$

The total volume is also obtained from the liquid level h_{level} and the geometry of the tank, which for a vertical cylinder is simply:

$$V_{liq} = \pi R^2 h_{level} \tag{3.3}$$

where R is the tank radius. By replacing the total liquid level with the height of a horizontal slice defined in eq 3.1, one obtains an expression for the total volume of that slice $V_{liq,i}$.

One important aspect of the model is the introduction of a growing *boundary layer thickness*, δ_i, which is defined as the thickness of the velocity boundary layer close to the tank wall. From Figure 3.2 it is evident that the volume of any liquid bulk element can be expressed as:

$$V_{LB,i} = \pi (R - \delta_i)^2 h_i \tag{3.4}$$

and from combining eq 3.2-3.4 it follows that any liquid boundary volume will be:

$$V_{LL,i} = \pi \delta_i (2R - \delta_i) h_i \tag{3.5}$$

This shows that every control volume is fully defined by the proportions of the tank and the thickness of the boundary layer.

The mass flow rate between liquid bulk elements, J_{LB}, is defined as positive in the direction away from the liquid/gas interface and towards the bottom of the tank. Similarly, the mass flow next to the wall, J_{LL}, has a positive direction towards the interface. Flow between the two sub-domains is defined to be positive when traveling from the bulk to the boundary layer, and is denoted J_{LBL}. Mass leaving and/or entering the liquid domain is represented by condensation flow rate J_{cond} (which is

naturally positive during net condensation and negative during net evaporation), and any potential filling/emptying of the tank, J_{out}. Similarly, venting of the ullage can be introduced via J_{vent}.

Empirical correlations

There are empirical expressions in literature derived to estimate the vertical mass flow brought on by convection close to a given surface. For a point at a vertical plate situated a certain distance from the tank bottom, one estimate for the flow rate is [12]:

$$J_{LL,i} = f(geo, i)\rho_i v_i \delta_i \begin{cases} 0.0833, & \text{if laminar } (Ra_i < 10^9) \\ 0.1436, & \text{if turbulent} \end{cases} \tag{3.6}$$

where ρ_i is the density of the LL element, v_i is the average local velocity of the boundary layer, and f is a function representing the horizontal distance along the wall segment (perimeter) for a given geometry. In the case of a vertical cylinder: $f = 2\pi R$ for all i. The flow rate is assumed laminar at low *Raleigh* numbers, which are the product of the *Grashof* and the *Prandtl* numbers, respectively:

$$Ra_i = Gr_i \cdot Pr \tag{3.7}$$

The Grashof number is defined as:

$$Gr_i = \frac{g\beta(T_{wall} - T_{LB,i})x_i^3}{\eta} \tag{3.8}$$

where g is the gravitational acceleration, β is the thermal compressibility of the liquid, x_i is the characteristic length (which in this case is the average height of the element counted from the tank bottom), and $\eta = \mu/\rho$ is the kinematic viscosity. The Prandtl number has the familiar definition: $Pr = \mu C_p/\kappa$, where C_p and κ are the specific heat capacity and thermal conductivity, respectively.

The average velocity of the boundary layer can be approximated as [23]:

$$v_i = 1.185 \frac{\eta}{x_i} \sqrt{\frac{Gr_i}{1 + 0.494 Pr^{2/3}}} \tag{3.9}$$

Finally, the velocity boundary layer thickness at a given horizontal slice and average height along the vertical wall can be estimated using eq 3.10 [23]. The velocity profile at the wall can be seen in Figure 3.3.

$$\frac{\delta_i}{x_i} = \begin{cases} 3.93 \left(\frac{0.952 + Pr}{Gr_i Pr^2} \right)^{1/4}, & \text{if laminar} \\ 0.565 \left(\frac{1 + 0.494 Pr^{2/3}}{Gr_i} \right)^{1/10}, & \text{if turbulent} \end{cases} \tag{3.10}$$

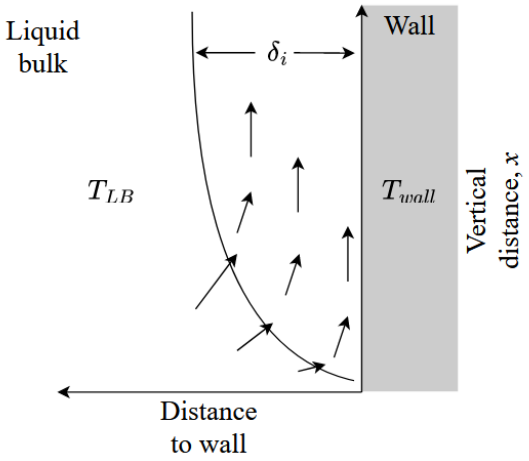

Figure 3.3 – Development of boundary layer close to tank wall.

If the Prandtl number is close to unity then it can be assumed that the thermal boundary layer δ_T (i.e., the distance from the wall at which the temperature is 99% of the free-stream temperature) is more or less equal to the velocity boundary layer [13]. Otherwise, if the flow profile is laminar, the thermal boundary layer can be estimated using the simple relation [24]:

$$\delta_T = \frac{\delta_i}{Pr^{1/3}} \tag{3.11}$$

However, it is the velocity boundary layer that defines the boundary control volumes, as mentioned earlier.

Mass and energy balances

Using the sign convention regarding the flow direction defined earlier, the general mass balance for control volumes at $i = \{2, \ldots, n-1\}$ for both sub-domains can be constructed accordingly:

$$\begin{aligned} \frac{d(m_{LB,i})}{dt} &= J_{LB,i+1} - J_{LB,i} - J_{LBL,i} \\ \frac{d(m_{LL,i})}{dt} &= J_{LL,i-1} - J_{LL,i} + J_{LBL,i} \end{aligned} \tag{3.12}$$

The first bulk control volume in contact with the bottom of the tank has no downwards facing vertical flow, and instead it is assumed that mass is transferred directly to the nearest boundary layer: $J_{LB,1} = J_{LL,1}$, and is therefore given by eq 3.6. Likewise, the top most layer ($i = n$) exchanges mass (and energy) with the interface:

$$\begin{aligned} \frac{d(m_{LB,1})}{dt} &= J_{LB,2} - J_{LL,1} - J_{out} \\ \frac{d(m_{LB,n})}{dt} &= J_{cond} + J_{LL,n-1} - J_{LB,n} \end{aligned} \tag{3.13}$$

Since the convective mass flows vertical to the wall (J_{LL}) are explicitly obtained using empirical correlations, the "flow field", i.e., the size of each mass flow entering and leaving a bulk control volume, can be obtained algebraically.

An energy balance for each control volume can be obtained using the first law of thermodynamics:

$$\begin{aligned} \frac{dU_{LB,i}}{dt} &= J_{LB,i+1}h_{LB,i+1} - J_{LB,i}h_{LB,i} - J_{LBL,i}h_{LBL,i} + \dot{W}_{LB,i} - h_{LB,i}\frac{dm_{LB,i}}{dt} \\ \frac{dU_{LL,i}}{dt} &= \dot{Q}_{WL,i} + J_{LL,i-1}h_{LL,i-1} - J_{LL,i}h_{LL,i} + J_{LBL,i}h_{LBL,i} + \dot{W}_{LL,i} - h_{LL,i}\frac{dm_{LL,i}}{dt} \end{aligned} \tag{3.14}$$

Here, the energy gain/loss due to work done on the control volume by compression/-

expansion of the fluid is represented by the term:

$$\dot{W}_{L(B,L),i} = -p\frac{dV_{L(B,L),i}}{dt} \tag{3.15}$$

The first and last liquid bulk control volumes are in direct contact with the tank wall and liquid-gas interface, respectively, meaning the heat flows across these boundaries must be included in the energy balances:

$$\begin{aligned}\frac{dU_{LB,1}}{dt} &= \dot{Q}_{WL,1} + J_{LB,2}h_{LB,2} - J_{LL,1}h_{LB,1} + \dot{W}_{LB,1} - h_{LB,1}\frac{dm_{LB,1}}{dt} \\ \frac{dU_{LB,n}}{dt} &= -\dot{Q}_{LS} + J_{cond}\Delta H_{vap} - J_{LB,n}h_{LB,n} + J_{LL,n-1}h_{LL,n-1} + \dot{W}_{LB,n} - h_{LB,n}\frac{dm_{LB,n}}{dt}\end{aligned} \tag{3.16}$$

where ΔH_{vap} is the latent heat of vaporation $(h_{vap}^{sat} - h_{liq}^{sat})$. The directions of all heat flows across different interfaces in the tank are defined according to Figure 3.4.

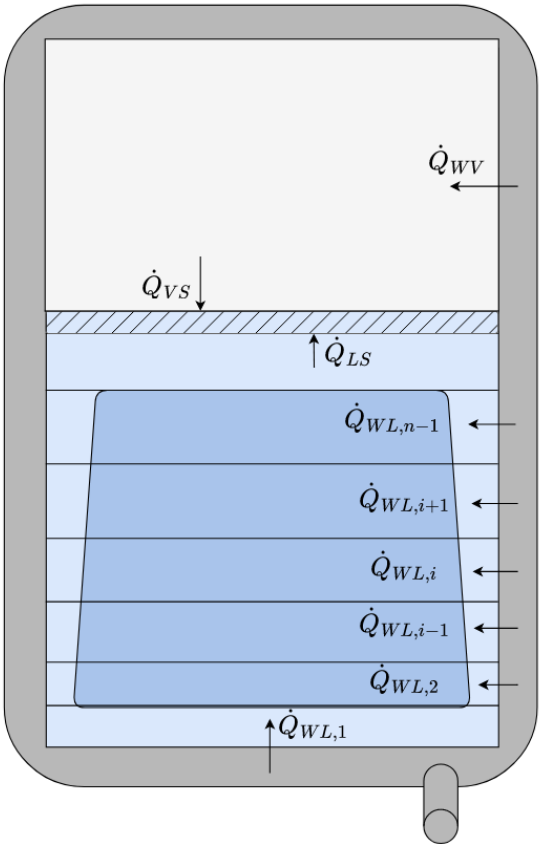

Figure 3.4 – Energy flow across tank walls and liquid-gas interface inside the storage tank.

The internal energy in each control volume is calculated from its mass and specific internal energy:

$$\Delta U_{L(B,L)i} = m_{L(B,L),i} \cdot \Delta u_{L(L,B),i} \tag{3.17}$$

Since thermal stratification as a phenomenon is primarily manifested in the liquid part of the tank it was deemed reasonable to model the vapor domain as one large control volume with homogeneous temperature. The mass and energy balances over the vapor domain are therefore simple to construct:

$$\begin{aligned} \frac{d(m_V)}{dt} &= -(J_{cond} + J_{vent}) \\ \frac{d(U_V)}{dt} &= \dot{Q}_{WV} - \dot{Q}_{VS} + \dot{W}_V - h_V \frac{dm_V}{dt} \end{aligned} \tag{3.18}$$

All fluid properties are calculated using a medium package for hydrogen already available in the Modelon VaporCycle library, as will be discussed later on in the report.

3.1.2 Gas - liquid interface

The mass and energy exchange across the interface between the two phases is a very important aspect of the model, and the temperature of the interface plays a direct role in determining the overall pressure in the ullage portion of the tank. To accurately estimate the driving force behind the phase exchange, the temperature gradient close to the surface on both sides of the interface is necessary. In this section, an approach of approximating the temperature gradient using optimal geometric grid finite volume discretisation is suggested.

In a number of articles written by Osipov and Viatcheslav et al. [25, 26] they argue that the interface between the two phases of cryogenic hydrogen can be viewed as a thin layer of saturated vapor with negligible mass. The temperature of the interface will therefore be equal to the saturation temperature T_s at a given pressure. A crass explanation is as follows: The low thermal conductivity of liquid hydrogen makes it so that the temperature of the interface between the two phases either rises or drops as latent heat from condensation/evaporation is absorbed/released at the interface. This continues until the condensation mass flow rate almost compensates the evaporation flow rate, leading to a phenomenon called condensation blocking. This entails that, despite there being highly non-equilibrium conditions inside the tank, there is still a type of quasi equilibrium at the interface. Because of this it is possible to introduce a mass-less, very thin film of saturated vapor as the interface [25, 26].

Optimal geometric grid finite volume discretisation

The following section contains a suggested approach on how to solve for the temperature gradient close to the film interface.

Assuming that the heat flow within a short distance from the interface is predominantly driven by thermal conduction, then the temperature profile Θ within that

spatial domain can be obtained by solving a straight forward thermal diffusion equation after application of Fourier's law:

$$\rho C_p \frac{\partial \Theta}{\partial t} = \kappa \frac{\partial^2 \Theta}{\partial x^2} \tag{3.19}$$

where C_p and κ are the heat capacity and thermal conductivity of the fluid, respectively, and with the initial value and boundary conditions:

$$\begin{aligned} \Theta(t = 0, x) &= T_{LB(v)}(0) \\ \Theta(t, x = 0) &= T_s(t) \\ \Theta(t, \infty) &= T_{LB,n}(t) \quad \text{or} \quad T_v(t) \end{aligned} \tag{3.20}$$

The above hyperbolic partial differential equation (PDE) can be solved numerically by discretizing it with respect to space. There are many discretization methods that could be used to do this, however, in this particular case the *finite volume method* (FVM) will be applied.

The first thing that needs to be done is defining and generating a mesh grid that will be used to divide the control volumes adjacent to the interface into k distinct sub-control volumes, here referred to as cells. The cell index $i \in \{1, \ldots, k\}$ is counted from the interface moving away into the bulk of each respective phase. For the sake of later calculations, a fictitious control volume (located at index 0) is also introduced as a representation for the film interface. The coordinate within a cell where state variables are solved is called a node, and the location of a node in relation to the other nodal points defines the mesh.

Ingerman and Druskin et al. [27] argues that the optimal grid spacing for numerical discretization of problems of this nature can be approached by applying a geometric progression using an exponential common ratio:

$$h_i = h_{i-1} e^{\frac{\pi}{\sqrt{k+1}}}, \quad i = 1, \ldots, k \tag{3.21}$$

where h_i in this case represents the distance between nodes in cells i and $i+1$. Here, $k+1$ is used in the common ratio as there are k cells + one fictitious "0:th" control volume. This will generate a grid that is very fine close to the interface and becomes more rough further out in the fluid, as is depicted in Figure 3.5.

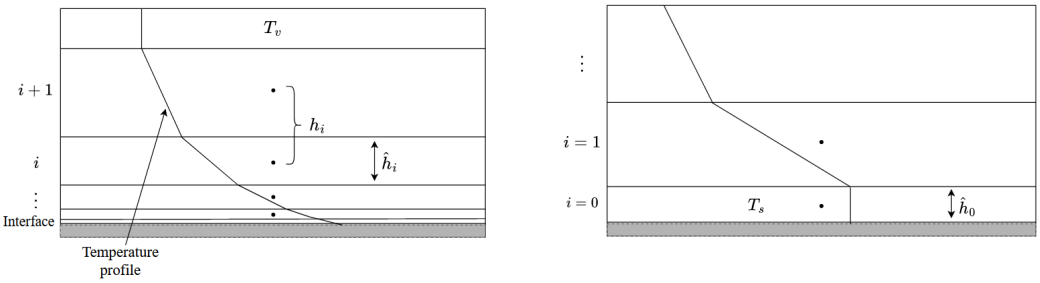

(a) Graphical representation of distance between cell nodes and cell length.

(b) Zoomed in view of interface in (a).

Figure 3.5 – Mesh grid for sub-control volumes close to the interface. Be aware that the actual placement of nodal points is not in the cell center.

To initialize the geometric progression we need to define the smallest distance between two nodes (i.e., between nodes 0 and 1) in the discretised cells. Any arbitrary value can be used, however, it can also be chosen in a way that gives it physical significance. Let h_0 represent the order of magnitude of the dimensions of a body being heated non-uniformly through conduction. Then it can be shown that [28]:

$$h_0 = \sqrt{\frac{\kappa\tau}{\rho C_p}} \tag{3.22}$$

where τ, referred to as the *relaxation time* for thermal conduction, is the time required for the temperature to become close to uniform throughout the body. This will be a parameter defined by the user of the model.

Combining eq 3.21 and eq 3.22 we get a general expression for the $i : th$ nodal distance in terms of the smallest distance:

$$h_i = \sqrt{\frac{\kappa\tau}{\rho Cp}} e^{\frac{\pi}{\sqrt{k+1}}i}, \quad i = 1, \ldots, k \tag{3.23}$$

Since eq 3.23 is a term from a geometric progression series, the sum of all terms in

the series will be:

$$\sum_{i=0}^{k} h_i = \sqrt{\frac{\kappa\tau}{\rho C_p}} \left(\frac{e^{\pi\sqrt{k+1}} - 1}{e^{\frac{\pi}{\sqrt{k+1}}} - 1} \right) \tag{3.24}$$

When applying this exponential scheme it is common to define the length $\hat{h}$ of each cell as the square root of the adjacent nodal length product [27]:

$$\hat{h}_i = \sqrt{h_i \cdot h_{i-1}} \tag{3.25}$$

which after substituting in eq 3.23 becomes:

$$\hat{h}_i = \sqrt{\frac{\kappa\tau}{\rho C_p}} e^{\frac{\pi(2i-1)}{2\sqrt{k+1}}} \tag{3.26}$$

The cell size of the fictitious control volume $\hat{h}_0$, (which in this case could be viewed as the thin mass-less layer of saturated vapor that makes up the interface) is defined as:

$$\hat{h}_0 = \frac{h_0}{1 + e^{\frac{\pi}{2\sqrt{k+1}}}} \tag{3.27}$$

The total length of the discretised sub-domain will therefore be:

$$\hat{h}_{tot} = \hat{h}_0 + \sum_{i=1}^{k} \hat{h}_i \tag{3.28}$$

where

$$\sum_{i=1}^{k} \hat{h}_i = \sqrt{\frac{\kappa\tau}{\rho C_p}} e^{-\frac{\pi}{2\sqrt{k+1}}} \left(\left(\frac{e^{\pi\sqrt{k+1}} - 1}{e^{\frac{\pi}{\sqrt{k+1}}} - 1} \right) - 1 \right) \tag{3.29}$$

Using the optimal grid, the energy equation can now be discretized with respect to space.

Discretization of energy equation

In order to properly derive an expression for the discretized energy equation in a cell, one needs to be re-familiarized with the Gauss' divergence theorem. The theorem states that the volume integral of the divergence of an arbitrary vector field $\boldsymbol{F}$ over a volume region is equal to the surface integral of the same field over the surface ∂S enclosing the region [29, 30]:

$$\iiint_{CV} (\nabla \cdot \boldsymbol{F}) dV = \oiint_{\partial S} (\tilde{\boldsymbol{n}} \cdot \boldsymbol{F}) dS \tag{3.30}$$

where $\tilde{\boldsymbol{n}}$ is the unit normal vector pointing outward from the surface.

The surface integral will be equal to the sum of integrals across all cell faces N_i of the $i : th$ control volume:

$$\oiint_{\partial S} (\tilde{\boldsymbol{n}} \cdot \boldsymbol{F}) dS = \sum_{\alpha=1}^{N_i} \oiint_{\partial S_\alpha} (\tilde{\boldsymbol{n}} \cdot \boldsymbol{F}) dS \tag{3.31}$$

To simplify calculations, evaluating the surface integral to approximately equal the surface area is common when using FVM:

$$\oiint_{\partial S_\alpha} (\tilde{\boldsymbol{n}} \cdot \boldsymbol{F}) dS \approx (\tilde{\boldsymbol{n}} \cdot \boldsymbol{F}) A_\alpha \tag{3.32}$$

where A_α is the surface area of the $\alpha : th$ face.

In the case of eq 3.19 there is only one spacial dimension, meaning each sub-control volume only has two faces ($N_i = 2$, $\alpha \in \{1, 2\}$). Likewise, the areas of these faces are simply the length of each respective face, which in the case of a vertical cylindrical tank will all be the same:

$$A_1 = A_2 = A$$

When considering other tank geometries and/or orientations, the above equality will likely no longer hold. However, given the fact that each step size $\hat{h}_i$ will be very small compared to the overall dimensions of the tank it is still a reasonable assumption to consider the areas of all faces to be approximately equal.

Integrating both sides of eq 3.19 over the volume of cell i and applying Gauss' divergence theorem on the right hand term yields:

$$\int_V \rho C_p \frac{\partial \Theta_i}{\partial t} dV = \oint_S \kappa \frac{\partial^2 \Theta_i}{\partial x^2} dS \tag{3.33}$$

With the convention that the flow field has a positive direction away from the interface towards the respective bulk phase, the surface integral on the right hand side in eq 3.33 can be evaluated using eq 3.31 and eq 3.32 to the following:

$$\oint_S \kappa \frac{\partial^2 \Theta_i}{\partial x^2} dS = -\kappa A_1 \frac{\partial \Theta_i}{\partial x}\bigg|_{\alpha=1} + \kappa A_2 \frac{\partial \Theta_i}{\partial x}\bigg|_{\alpha=2} \tag{3.34}$$

Utilizing the area equality and assuming that the thermal conductance is constant throughout the cell leaves us with the final expression:

$$\rho C_p \frac{\partial \Theta_i}{\partial t} \Delta V = \kappa A \left(\frac{\partial \Theta_i}{\partial x}\bigg|_{\alpha=2} - \frac{\partial \Theta_i}{\partial x}\bigg|_{\alpha=1} \right) \tag{3.35}$$

From figure 3.5 it can be seen that ΔV for a given cell can be evaluated as:

$$\Delta V = A \cdot \hat{h}_i \tag{3.36}$$

which, given that the facial areas are the same, means that the actual geometrical expression for the area is inconsequential to the energy equation, since it appears on both sides of the equation.

Next is the approximation for the first order spacial derivative of the temperatures at the cell faces. This can be done using a simple first order forward finite difference [29], considering the values at the nodal points upstream and downstream of the cell

face in question and the distance between them:

$$\left.\frac{\partial \Theta_i}{\partial x}\right|_{\alpha=2} \approx \frac{\Theta_{i+1} - \Theta_i}{h_i} \tag{3.37}$$

Finally, after rearrangement of equation 3.35 and approximating the fluxes through the cell faces using eq 3.37 one arrives at the discretised energy equation for each interfacial cell volume:

$$\frac{\partial \Theta_i}{\partial t} = \frac{\kappa}{\hat{h}_i \rho C_p} \left(\frac{\Theta_{i+1} - \Theta_i}{h_i} - \frac{\Theta_i - \Theta_{i-1}}{h_{i-1}} \right) \tag{3.38}$$

The equation has now been reduced to a much more manageable form differentiated only with respect to time. Using the boundary conditions in eq 3.20 we can write the discretised equation on matrix form:

$$\begin{bmatrix} \dot{\Theta}_1 \\ \dot{\Theta}_2 \\ \vdots \\ \dot{\Theta}_k \end{bmatrix} = \mathcal{D} \begin{bmatrix} \Theta_1 \\ \Theta_2 \\ \vdots \\ \Theta_k \end{bmatrix} + \mathcal{B} \begin{bmatrix} T_s \\ \\ T_{LB,n(v)} \end{bmatrix} \tag{3.39}$$

where $\mathcal{D}$ and $\mathcal{B}$ can be called the discretization matrix and boundary matrix, respectively. It can be shown that the resulting $\mathcal{D}$ will be diagonally dominant.

$$\mathcal{D} = \begin{bmatrix} -\beta_1 & \alpha_1 & 0 & 0 & \dots & 0 \\ \alpha_1 & -\beta_2 & \alpha_2 & 0 & \dots & 0 \\ 0 & \alpha_2 & -\beta_3 & \alpha_3 & \dots & 0 \\ 0 & 0 & \alpha_3 & -\beta_4 & \ddots & \vdots \\ \vdots & \vdots & \vdots & \ddots & \ddots & \alpha_{k-1} \\ 0 & 0 & \dots & 0 & \alpha_{k-1} & -\beta_k \end{bmatrix} \qquad \mathcal{B} = \begin{bmatrix} \alpha_0 & 0 \\ 0 & 0 \\ \vdots & \vdots \\ \vdots & \vdots \\ 0 & 0 \\ 0 & \alpha_k \end{bmatrix} \tag{3.40}$$

where:

$$\begin{aligned} \alpha_i &= \frac{1}{h_i} \frac{\kappa}{\hat{h}_i \rho C_p} \\ \beta_i &= \left(\frac{1}{h_i} + \frac{1}{h_{i-1}} \right) \frac{\kappa}{\hat{h}_i \rho C_p} \\ i &= 0, \dots, k \end{aligned} \tag{3.41}$$

With the help of the temperature gradient close to the interface, general expressions describing the mass and energy exchange between the fluid and interface – and therefore ultimately between the two phases – can now be constructed.

Interface mass-and heat transfer

To derive an expression for the heat transfer between the fluid phases and interface, $\dot{Q}_{LS}$ and $\dot{Q}_{VS}$, we can again assume that these are due mainly to conduction and that the local energy flux at the surface of the interface is described by Fourier's law:

$$q_{LS} = \frac{-\dot{Q}_{LS}}{A_{LV}} = -\kappa \frac{\partial \Theta}{\partial x}\bigg|_{x=0} \tag{3.42}$$

where A_{LV} is the surface area of the liquid-gas interface. Note that the sign in front of $\dot{Q}_{LS}$ stems from its defined positive direction (see Figure 3.4). Similar to before

we can approximate the spacial derivative using forward finite difference (eq 3.37) where the temperature of the interface is equal to the saturation temperature:

$$\left.\frac{\partial \Theta}{\partial x}\right|_{x=0} \approx \frac{\Theta_1 - T_s}{h_0} \tag{3.43}$$

Inserting the above expression into eq 3.42 yields:

$$\frac{\dot{Q}_{LS}}{A_{LV}} = \kappa \left(\frac{\Theta_1 - T_s}{h_0}\right) \Longleftrightarrow \dot{Q}_{LS} = \alpha_{cond} A_{LV} \left(\Theta_1 - T_s\right) \tag{3.44}$$

where

$$\alpha_{cond} = \frac{\kappa}{h_0} = \sqrt{\frac{\kappa \rho C_p}{\tau}} \tag{3.45}$$

The exact same procedure is applied to get the vapor heat transfer.

If the assumption is made that the film interface is so thin that its mass can be neglected, then the energy balance over the interface can be written as [25]:

$$\dot{Q}_{LS} + \dot{Q}_{VS} + J_{cond} \Delta H_{vap} = \frac{d(m_f u_f)}{dt} = 0 \tag{3.46}$$

which means that the condensation flow rate can now be obtained via:

$$J_{cond} = -\frac{(\dot{Q}_{LS} + \dot{Q}_{VS})}{\Delta H_{vap}} \tag{3.47}$$

3.1.3 Wall heat transfer – free convection model

The heat ingress into the liquid and gas domains from the environment through the tank walls can be obtained by applying *Newton's law of cooling* on the different wall sections in contact with fluid. The general expression can be written as:

$$\dot{Q}_{WL(v),i} = \alpha_i A_i (T_{wall} - T_{i,\infty}) \tag{3.48}$$

where A_i is the heat transfer area at a certain wall section and $T_{i,\infty}$ is the fluid temperature (gas or liquid) far from the wall normal to its surface. The heat transfer coefficient can be written as:

$$\alpha_i = \frac{\kappa}{x_i}\overline{Nu_i} \tag{3.49}$$

where the average Nusselt number can be estimated using empirical correlations depending on the geometry.

For an arbitrary horizontal slice of the tank, the heat transfer rate into the liquid boundary layer control volume can be calculated as:

$$\dot{Q}_{WL,i} = \alpha_i A_{WL,i}(T_{wall} - T_{LB,i}) \tag{3.50}$$

with $A_{WL,i} = 2\pi R h_i$ for all i. Using the Nusselt number for free convection at a vertical wall [31], the heat transfer coefficient can be obtained via the expression:

$$\alpha_i = \frac{\kappa}{x_i}\begin{cases} 0.68 + 0.503\left(Ra_i\Psi\right)^{1/4}, & 10^5 < Ra_i < 10^9 \\ 0.15\left(Ra_i\Psi\right)^{1/3}, & 10^9 < Ra_i < 10^{11} \end{cases} \tag{3.51}$$

where the characteristic length x_i is the same as in eq 3.8. The dimensionless factor Ψ in eq 3.51 is defined as:

$$\Psi = \left(1 + \left(\frac{0.492}{Pr}\right)^{9/16}\right)^{-16/9} \tag{3.52}$$

The assumption that the convection at the cylindrical vertical wall can be described using eq 3.51 is reasonable provided that the curvature effect of the cylinder is not too significant. This is true when the boundary layer thickness is small in relation to the cylindrical diameter D, which can be expressed as [32]:

$$\frac{D}{L} \geq \frac{35}{Gr^{1/4}} \tag{3.53}$$

For the circular bottom wall segment in contact with the first LB control volume the area will be $A_{WL,1} = \pi R^2$, and the heat transfer coefficient α_{bot} can be estimated using the Nusselt number at a horizontal surface [31]. Here, the characteristic length equal to the tank radius R is used to calculate the Raleigh number from eq 3.7-3.8:

$$\alpha_{bot} = \frac{\kappa}{R} \begin{cases} 0.54 Ra_R^{1/4} & 10^4 < Ra_R < 10^7 \\ 0.15 Ra_R^{1/3}, & 10^7 < Ra_R < 10^{11} \end{cases} \tag{3.54}$$

3.2 Alternative tank orientations and geometries

In practical applications, a vertically oriented cylinder might not always be the most optimal means of storing liquid hydrogen. It is therefore important that the proposed model has some flexibility when it comes to the type of tank shape that the user would like to employ. Different geometric and positional augmentations to the storage tank have been developed in a replaceable package that the user of the model can easily specify to their liking through the Modelon Impact graphical user interface.

This section will cover in detail how two very common tank designs: horizontal cylinders with flat and hemispherical ends, respectively, are implemented to be compatible with the many horizontal control volumes introduced for the liquid phase. The reason these shapes takes precedence is that they are a very likely choice for tank design of cryogenic liquid vessels [1].

3.2.1 Horizontal cylinder

Although orienting the tank horizontally may seem to be a minor alteration to that of a vertical tank, making modifications to the model to represent this still requires some thought.

Flat ends

The perhaps most straightforward case is simply orienting the tank horizontally while retaining its flat ends. From geometry it is easily shown that the total volume of liquid inside a horizontal cylinder filled to the level h_{level} can be obtained from:

$$V_{liq} = L\left(R^2 cos^{-1}\left(\frac{R - h_{level}}{R}\right) - (R - h_{level})\sqrt{R^2 - (R - h_{level})^2}\right) \tag{3.55}$$

For the sake of convenience, let us introduce the intermediate geometric variable

$$y_i = h_i \cdot i - R, \qquad i \in \{1, \ldots, n\}$$

where h_i is the constant control volume height defined in eq 3.1 (Section 3.1.1). Using this, the volume of any horizontal liquid layer slice at index $i \in \{2, \ldots, n\}$ can be expressed as the difference between two volumes given by eq 3.55 evaluated at i and $i - 1$, respectively:

$$\begin{aligned} V_{liq,i} = {} & L\left(R^2 cos^{-1}\left(-\frac{y_i}{R}\right) + y_i\sqrt{R^2 - y_i^2}\right) \\ & - L\left(R^2 cos^{-1}\left(-\frac{y_{i-1}}{R}\right) + y_{i-1}\sqrt{R^2 - y_{i-1}^2}\right) \end{aligned} \tag{3.56}$$

Just like in the vertical tank, the liquid sub-domain volumes V_{LB} and V_{LL} are dependent on the growth of the boundary layer thickness δ_i. At the flat end sections of the horizontal tank, δ_i can be assumed to grow in the same way as depicted in Figure 3.2b (i.e., as distinct rectangles protruding into the liquid bulk). However, this approach should not be used for the cylindrical wall sections as this will introduce errors for larger values of h_i. It is therefor more appropriate to define the

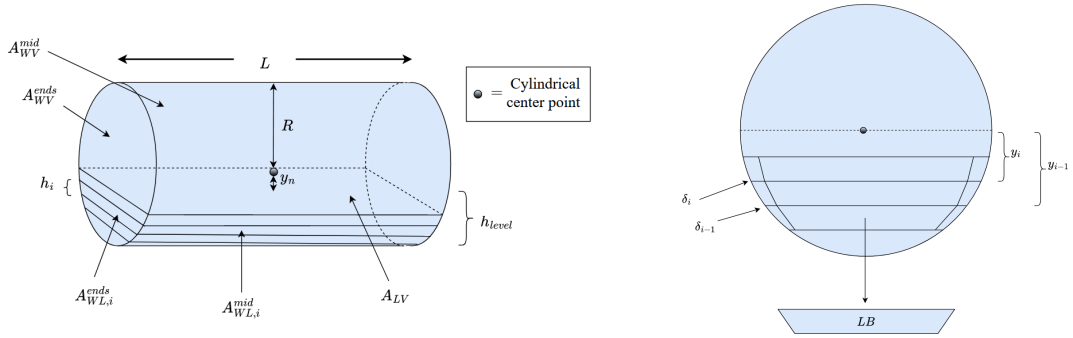

(a) Horizontal cylindrical tank with flat ends.

(b) Cross-sectional slice of horizontal tank middle segment.

Figure 3.6 – Schematic depiction of a horizontally oriented cylindrical tank filled to a certain level of fluid.

starting-point of δ_i as the end point of δ_{i-i}, etc. This will lead to the enclosed liquid bulk volumes $V_{LB,i}$ having a trapezoidal shape when viewed cross-sectionally, as is shown in Figure 3.6b. When expanding to three dimensions the bulk volume then becomes a so-called trapezoidal prism.

It can be shown that the volume of the trapezoidal prism delimited by the growing boundary layer is equal to:

$$V_{LB,i} = \left(\sqrt{R^2 - y_i^2} + \sqrt{R^2 - y_{i-1}^2} - (\delta_1 + \delta_{i-1}) \right) (L - 2\delta_i) h_i \tag{3.57}$$

The volume of the boundary layer control volumes can now be obtained by taking the difference between the total volume of the slice and that of the bulk liquid:

$$V_{LL,i} = V_{liq,i} - V_{LB,i} \tag{3.58}$$

The area between liquid and vapor at the interface is obtained in a similar manner as the volume expressions:

$$A_{LV} = 2\sqrt{R^2 - y_n^2}L, \qquad y_n = h_{level} - R \tag{3.59}$$

Just like for the simple vertical cylinder case presented in Section 3.1.1, the area between the wall and the fluid is important when calculating the heat flow into the tank. Since there will now be more then one type of geometry of the wall in contact with the liquid boundary layer, the heat flow into said layer will be different at different parts of the tank. At the flat end sections of the horizontal cylinder, the total area for a given horizontal slice can be derived from the volume of said slice and the length of the tank:

$$A_{WL,i}^{ends} = 2 \cdot \frac{V_{liq,i}}{L} \tag{3.60}$$

The area of the middle cylindrical section of the tank, or truncated lateral surface area, can be calculated from:

$$A_{WL,i}^{mid} = 2R\left(cos^{-1}\left(-\frac{y_i}{R}\right) - cos^{-1}\left(-\frac{y_{i-1}}{R}\right)\right)L \tag{3.61}$$

Having the wall/liquid areas, calculating the wall/vapor areas is a trivial matter:

$$\begin{aligned} A_{WV}^{ends} &= 2\pi R^2 - \sum_{i=1}^{n} A_{WL,i}^{ends} \\ A_{WV}^{mid} &= 2\pi RL - \sum_{i=1}^{n} A_{WL,i}^{mid} \end{aligned} \tag{3.62}$$

The heat flow into a given boundary layer control volume is calculated as the sum of contributions from the end- and mid sections:

$$Q_{WL,i} = (\alpha_i^{ends} A_{WL,i}^{ends} + \alpha_i^{mid} A_{WL,i}^{mid})(T_{wall} - T_{LB,i}) \tag{3.63}$$

α_i^{ends} is given by eq 3.51 and α_i^{mid} is calculated using the average Nusselt number for a horizontal cylinder [31]:

$$\alpha_i^{mid} = \frac{\kappa}{x_i} \left\{ 0.60 + \frac{0.387 Ra_i^{1/6}}{[1 + (0.559/Pr)^{9/16}]^{8/27}} \right\}^2 \tag{3.64}$$

For the sake of simplicity it is assumed that eq 3.6 – 3.10 describing the convective flow rate and boundary layer next to the tank wall are still valid for the horizontal tank, and that only the function f in eq 3.6 changes depending on the geometry. For a horizontal cylinder with flat ends, f is evaluated as:

$$f(HorizontalCylinder, i) = 2L + 4\sqrt{R^2 - y_i^2} \tag{3.65}$$

Hemispherical ends

The end sections of the storage tank do not necessarily have to be flat, and one alternative design choice is to instead have hemispherical or elliptical ends. Essentially, this is like taking the tank with flat ends in Figure 3.6a and adding half of an ellipsoid onto each end assuming that the ends are symmetrical. A principle sketch of this design can be seen in Figure 3.7.

When deriving expressions for the relevant variables in this geometry, it is simpler to look at the respective contributions from the cylindrical and elliptical parts separately and later combine them. The two elliptical ends can be treated as one whole ellipsoid, and everything related to the cylindrical part was discussed in the previous

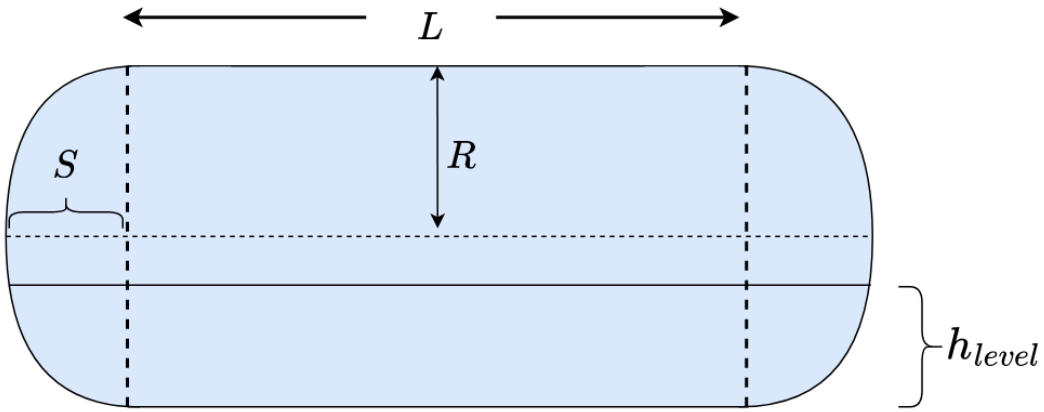

Figure 3.7 – Horizontally oriented storage tank with hemispherical ends and fill level h_{level}. It is assumed that the ends are symmetrically proportioned with S being the elliptical center distance from the cylinder.

section.

Again, let us define some intermediate geometric variables in order to simplify later calculations.

$$
\begin{aligned}
x_i &= 2R - h_i \cdot i \\
r_i &= \sqrt{R^2 - y_i^2} - \delta_i \\
s_i &= S\sqrt{1 - \left(\frac{y_i}{R}\right)^2} - \delta_i
\end{aligned}
$$

The graphical representation of these variables can be seen in Figure 3.8. The volume of the liquid domain in an ellipsoid with the fill level h_{level} is obtained from:

$$
V_{liq}^{ellipsoid} = \frac{4}{3}\pi R^2 S - \frac{\pi S}{3R} x_n^2 (3R - x_n) \tag{3.66}
$$

Therefore, the volume of any horizontal liquid layer slice at index $i \in \{2, \ldots, n\}$ can be expressed as the difference between two volumes given by eq 3.66 evaluated at i

and $i-1$, respectively. After some work this equates to:

$$V_{liq,i}^{ellipsoid} = \frac{\pi S}{3R}\left(x_{i-1}^2(3R - x_{i-1}) - x_i^2(3R - x_i)\right) \tag{3.67}$$

Figure 3.8 shows that the liquid bulk control volume enclosed by δ_i in the elliptical part will take the shape of a truncated elliptical cone. The volume of said cone can be calculated from:

$$V_{LB,i}^{ellipsoid} = \frac{\pi r_{i-1}}{3s_{i-1}} h_i \left(s_{i-1}^2 + s_{i-1}s_i + s_i^2\right) \tag{3.68}$$

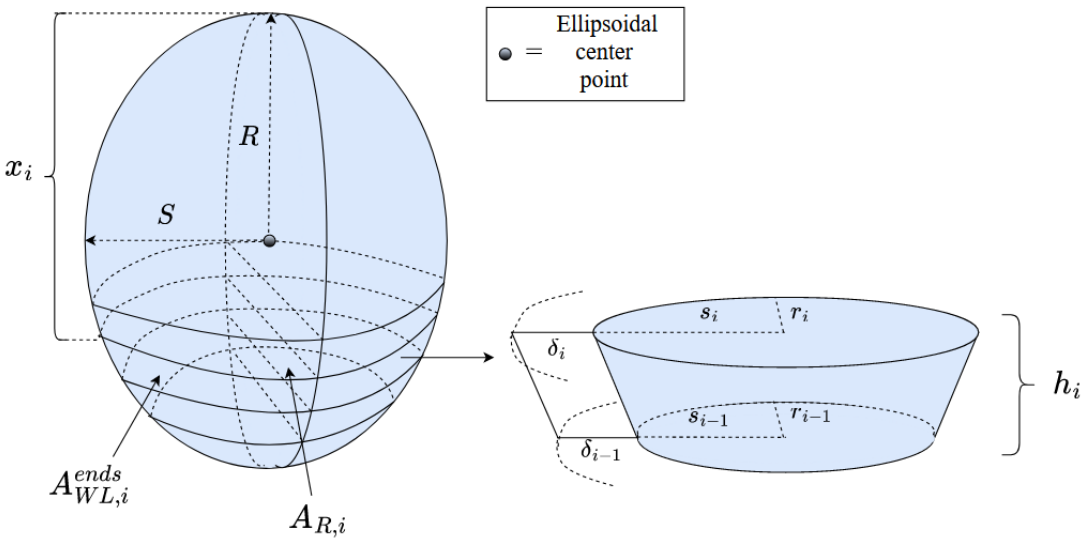

Figure 3.8 – 3D ellipsoid created from the elliptical ends of the tank and the resulting truncated cone representing the liquid bulk control volume. $A_{WL,i}^{ends}$ is the truncated elliptical surface area at index i, and $A_{R,i}$ is the truncated circular vertical cross-sectional area.

As always, the volume of the liquid boundary layer can now be obtained by simply subtracting eq 3.68 from eq 3.67. The volumes for the cylindrical part, $V_{liq,i}^{cyl}$ and $V_{LL,i}^{cyl}$ are calculated using eq 3.56 and 3.58, respectively. $V_{LB,i}^{cyl}$ is almost the same as in eq 3.57, with the slight modification to the "length" term since there is no boundary layer protruding into the cylinder from the ends:

$$V_{LB,i}^{cyl} = \left(\sqrt{R^2 - y_i^2} + \sqrt{R^2 - y_{i-1}^2} - (\delta_1 + \delta_{i-1}) \right) L h_i \tag{3.69}$$

The total volume of all control volumes is now determined as the sum of ellipsoid and cylindrical contributions:

$$\begin{aligned} V_{LB,i} &= V_{LB,i}^{ellipsoid} + V_{LB,i}^{cyl} \\ V_{LL,i} &= V_{LL,i}^{ellipsoid} + V_{LL,i}^{cyl} \end{aligned} \tag{3.70}$$

The surface area at the interface between liquid and gas will be:

$$A_{LV} = 2\sqrt{R^2 - y_n^2} L + \pi S R \left(1 - \left(\frac{y_n}{R} \right)^2 \right) \tag{3.71}$$

Obtaining the surface area for the horizontal slices of the ellipsoid $A_{WL,i}^{ends}$ is not as straight forward. The total surface area of an ellipsoid can be calculated from [33]:

$$A_{ellipsoid} = \begin{cases} 2\pi R^2 + \frac{\pi S^2}{e} \ln \frac{1+e}{1-e}, & \text{if oblate} \quad (S < R) \\ 2\pi R^2 \left(1 + \frac{S}{eR} \arcsin e \right), & \text{if prolate} \quad (S > R) \end{cases} \tag{3.72}$$

where e is the *eccentricity* of the ellipse:

$$e = \begin{cases} \sqrt{1 - \left(\frac{S}{R} \right)^2}, & \text{if oblate} \\ \sqrt{1 - \left(\frac{R}{S} \right)^2}, & \text{if prolate} \end{cases} \tag{3.73}$$

Expressing the exact surface area of the horizontal slice at index i analytically

requires a fare amount of calculus and is surprisingly complicated. Instead, let us assume that the ratio between horizontal slice and total ellipsoid surface area is approximately the same as the ratio between the horizontal slice and total area of the 2D circle inscribed withing the ellipsoid (see Figure 3.8):

$$\frac{A_{WL,i}^{ends}}{A_{ellipsoid}} \approx \frac{A_{R,i}}{\pi R^2} \tag{3.74}$$

where:

$$A_{R,i} = \left(R^2 cos^{-1}\left(-\frac{y_i}{R}\right) + y_i\sqrt{R^2 - y_i^2}\right) - \left(R^2 cos^{-1}\left(-\frac{y_{i-1}}{R}\right) + y_{i-1}\sqrt{R^2 - y_{i-1}^2}\right) \tag{3.75}$$

This means that an approximate expression of the surface area of interest can now be written as:

$$A_{WL,i}^{ends} \approx A_{ellipsoid}\left(\frac{A_{R,i}}{\pi R^2}\right) \tag{3.76}$$

$A_{WL,i}^{mid}$ is of course the same as before and obtained through eq 3.61. The wall-vapor areas are now easily determined:

$$\begin{aligned} A_{WV}^{ends} &= A_{ellipsoid} - \sum_{i=1}^{n} A_{WL,i}^{ends} \\ A_{WV}^{mid} &= 2\pi RL - \sum_{i=1}^{n} A_{WL,i}^{mid} \end{aligned} \tag{3.77}$$

The heat flow into a given boundary layer is calculated using the same formula

described in eq 3.63, with the heat transfer coefficient α_i^{mid} being the same as in the previous section (see eq 3.64). α_{ends} can be estimated using the average Nusselt number at a spherical wall [31]:

$$\overline{Nu}_i = 2 + \frac{0.589 Ra_i^{1/4}}{[1 + (0.496/Pr)^{9/16}]^{4/9}} \tag{3.78}$$

Finally, using Ramanujan's first approximation for the perimeter of an ellipse [34], an expression for the geometric function f used to estimate the vertical flow rate at the tank wall in eq 3.6 can be obtained according to:

$$f(HorizontalCylinderEllipsoid, i) = 2L + \pi \left[3(s_i + r_i) - \sqrt{(3s_i + r_i)(s_i + 3r_i)}\right] \tag{3.79}$$

The relative complexity of f has so far increased for each tank geometry. A summery of all derived expressions of f for the main geometries can be found in Table 3.1.

Table 3.1 – Geometric perimeter function for the three main geometrical considerations.

Tank shape	$f(geo, i)$
Vertical Cylinder:	$2\pi R$
Horizontal Cylinder flat:	$2L + 4\sqrt{R^2 - y_i^2}$
Horizontal Cylinder ellipsoid:	$2L + \pi \left[3(s_i + r_i) - \sqrt{(3s_i + r_i)(s_i + 3r_i)}\right]$

3.2.2 Other geometries

Other potential tank shapes that might be of interest have also been implemented, or will likely be in the near future. These include:

- Vertical cylinder with hemispherical ends
- Horizontal and vertical cylinders with one hemispherical end

- Rectangular cuboid tank

A thorough derivation of the expressions for these shapes is not presented in this report, as they can be derived using the same methods found in the above sections.

3.3 Dynamic wall model

A dynamic wall model was implemented for the storage tank so that the the change in surface temperature of the wall in contact with fluid T_{wall} over time could be estimated. The wall was divided into two distinct control volumes: one for the wet wall in contact with liquid; and one for the dry wall in contact with vapor. Direct heat transfer through conduction between the two wall segments was, for the sake of simplicity, assumed to be negligible.

The mass of the wet and dry walls are calculated from the density of the wall and the volume of wall in contact with each respective phase:

$$\begin{aligned} m_{WL} &= V_{WL}\rho_{wall} \\ m_{WV} &= V_{WV}\rho_{wall} \end{aligned} \tag{3.80}$$

The wall volumes will of course depend on tank geometry and current fill level, and are obtained using approaches similar to Section 3.2 in the geometry package.

Assuming that the temperature of the outside of the wall is the same as the ambient temperature, then the total heat transfer rate into e.g., the wet wall segment due to thermal conduction can be modeled as [2]:

$$\dot{Q}_{EW,L} = \frac{\kappa_{wall}}{x_{wall}} \frac{A_{e,liq}}{A_{o,liq}} (T_{external} - T_{wall}); \qquad A_{e,liq} = \frac{A_{o,liq} - A_{i,liq}}{\ln\left(\frac{A_{o,liq}}{A_{i,liq}}\right)} \tag{3.81}$$

where κ_{wall} and x_{wall} are the thermal conductivity and wall thickness, respectively; A_e is the effective heat exchange surface area, and A_i and A_o are the inner and

outer tank wall areas. A rudimentary energy balance over the wet wall can now be constructed according to:

$$C_{p,W}\frac{d(mT)_W}{dt} = C_{p,W}\left(m_W\frac{dT_W}{dt} + T_W\frac{dm_W}{dt}\right) = \dot{Q}_{EW,L} - \sum_{i=1}^{n}\dot{Q}_{WL,i} \tag{3.82}$$

which after some rearrangement becomes:

$$\frac{dT_{WL}}{dt} = \frac{1}{C_{p,W}m_{WL}}\left(\dot{Q}_{EW,L} - \sum_{i=1}^{n}\dot{Q}_{WL,i}\right) - \frac{T_{WL}}{m_{WL}}\frac{m_{WL}}{dt} \tag{3.83}$$

The exact same derivation applies to the vapor dry wall segment. This very simple dynamic wall model is mainly intended as a placeholder while testing the overall tank model. A more comprehensive wall model compatible with discretization is currently under development for the Modelon ThermoFluid library that would be more appropriate for later implementation.

3.4 Calculation of fluid properties

One noteworthy implementation to the developed model is that it takes into account the state dependent properties of the fluid, as opposed to assuming them being constant throughout a dynamic simulation. This means that the physical behavior of a control volume can be uniquely distinct from neighboring ones. The different physical and thermodynamic properties of the hydrogen fluid are obtained through the medium package available in the Modelon VaporCycle library. This replaceable package makes it convenient to specify and calculate all relevant properties pertaining to a number of fluids based on the pressure and specific enthalpy state variables of the system. As such, properties like density, thermal conductivity, heat capacity and specific internal energy are easily obtained. Naturally, this also determines the phase (liquid or gas) of the fluid inside of a control volume at any given point, as well as the proportions of each phase in a two phase system if one was to emerge.

It should also be mentioned that the compatibility with built-in medium libraries makes it possible to use the tank model for simulation of fluids other than hydrogen. The equations and assumptions used by the medium package for hydrogen are based on work done by B. A. Younglove [35]. Some of these can be found in Appendix A.1.

3.5 Additional model implementations

Since the medium package uses state variables such as enthalpy to determine the phase of the hydrogen inside of a control volume, there is a chance that some amount of liquid within e.g., a LL control volume will change into the gaseous phase if the enthalpy $h_{LL,i}$ exceeds the saturation enthalpy $h_{liq}^{sat}(p)$ at a certain pressure. This is essentially equivalent to liquid boiling close the the tank wall. If this happens, the fluid properties inside said control volume will be calculated for a two phase system mixture of liquid and gas, which could lead to undesirable results if not addressed. Of course, the same is also true for liquid condensate inside of the vapor control volume.

In a real physical system, gas bubbles formed in the liquid at the walls would simply rise to the surface through buoyancy and enter the gas phase. Here, a simplified representation of this phenomenon has been implemented by estimating the mass flow rate of gas in the liquid phase to the gas phase (and vise versa) by considering the fraction of gas present in each control volume. Note that this is a different transport than the condensation flow rate J_{cond} introduced in section 3.1.2. For simplicity it is assumed that transport from one liquid control volume does not effect neighboring control volumes, and that the transport is instantaneous.

The option to include these "bulk" evaporation and condensation phenomena can be freely set by the user of the model. If this option is active, then the mass and energy balances presented in eq 3.12 – 3.18 will be modified to also include the terms:

$$
\begin{aligned}
J_{LB,i}^{evap} &= \frac{x_{LB,i}\rho_i V_{LB,i}}{\tau_{evap}} \\
J_{LL,i}^{evap} &= \frac{x_{LL,i}\rho_i V_{LL,i}}{\tau_{evap}} \\
J_{v}^{cond} &= \frac{(1-x_v)\rho_i V_{LB,i}}{\tau_{cond}}
\end{aligned}
\tag{3.84}
$$

where $x_{LB,i}$, $x_{LL,i}$ and x_v are the *steam qualities* of the respective control volumes, and τ_{cond}, τ_{evap} are time constants for bulk evaporation and condensation, respectively. As mentioned before, the steam qualities describe the fraction of gas in either phase, and are estimated based on the enthalpy inside of the control volume. The exact algorithm as implemented in modelica code can be found in Appendix A.2. Likewise, the extended mass and energy balances after implementation of bulk evaporation and condensation mass flows can be found in Appendix A.2.

3.6 Simulation of model

When executing the model in Modelon Impact, all code is compiled and the various equations are symbolically manipulated into a flat modelica structure where all the hierarchy is removed. It is also at this stage that potential state variables are selected by the compiler before simulating the model. The state variables are variables within a set of equations capable of describing the state of a system in enough detail to determine the future behavior of that system. Since all of the fluid properties of hydrogen can be determined using pressure and specific enthalpy, these variables were manually declared to be preferred state variables using the built-in modelica definition `StateSelect.prefere`. The same was done for the tank fill level h_{level}, as this state plays a crucial role in the different geometry models when calculating all the different volumes as described in Section 3.2.

Another important compilation step is *Tearing*, which is when the compiler decides what variables need to be solved through iteration. This is often required when there are large non-linear algebraic equation systems that can not be solved analytically. In the proposed model, the state derivatives of pressure and specific enthalpy will be iteration variables, as it is not possible to solve the many mass and energy balances in all control volumes simultaneously without iteration. So will the state derivative

of h_{level}, since volume also is part of these non-linear equation systems.

Once all the associated compilation steps are complete, the modelica code is converted into C-code and simulated using one of several dynamic solvers available via the Modelon Impact user interface. The stiff and non-stiff solver CVode was used for all simulations presented throughout the following sections of this thesis. For a much more comprehensive explanation of the different steps involved in the conversion of a modelica model to a simulation model, please consult the Modelon Help Center at `https://help.modelon.com` [36].

4 Result and Discussion

4.1 Model validation

To see whether or not the implemented model is able to produce trustworthy simulation results, it needs to be validated and compared to experimentally observed data. The perhaps most prominently referenced source across literature regarding boil-off and self-pressurization in a liquid hydrogen tank is the study conducted by Hasan et. al at NASA's Glenn Research Centre [3], the same source from which the pressure measurements showcased in Figure 2.1 were obtain.

In their study, Hasan et al. used an experimental set-up consisting of a 4.89 m^3 ellipsoidal storage tank insulated with two blankets of *multi-layered* insulation with unspecified thickness, each blanket having 17 layers of Mylar. At the start of the experiments the fill level was in the range of 83-85% on the basis of tank volume, and the total duration of the test was 98.5 h. However, for our purposes only the first 14 hours are of interest as by this point steady-state conditions had long since been achieved. Pressure and temperature inside of the tank was measured during two experiments with different starting conditions: Isothermal and Steady Boil-off. For a recap of these, please see Section 2.1.2.

Here, the tank was modeled as a perfect sphere by using the HorizontalCylinderEllipsoid geometry model and setting $L = 0$ with $S = R$. The inner radius of the tank was set to 1.05 m. The number of horizontal liquid layers n was set to 10, and the space close to the interface was discretized into $k = 3$ cells on both the liquid and vapor side. Isothermal starting conditions were simulated by initializing the model using liquid and ullage starting temperatures reported in the experiment, with no mass transfer in terms of filling or emptying of liquid or venting of gas. Steady Boil-off conditions, as mentioned in section 2.1.2, are obtained after some time is allowed to pass while venting the storage tank in order to achieve steady-state conditions, after which self-pressurization is engaged by closing the venting valve. This was simulated by connecting the tank model to a valve component operated by an

on-off actuator, whose state is determined by a temperature sensor output. These additional components are conveniently found in the Modelon ThermoFluid library. The principle setup can be seen in Figure 4.1. The system enters into steady-state at a vapor temperature of 35 K reportedly achieved after about 4 hours.

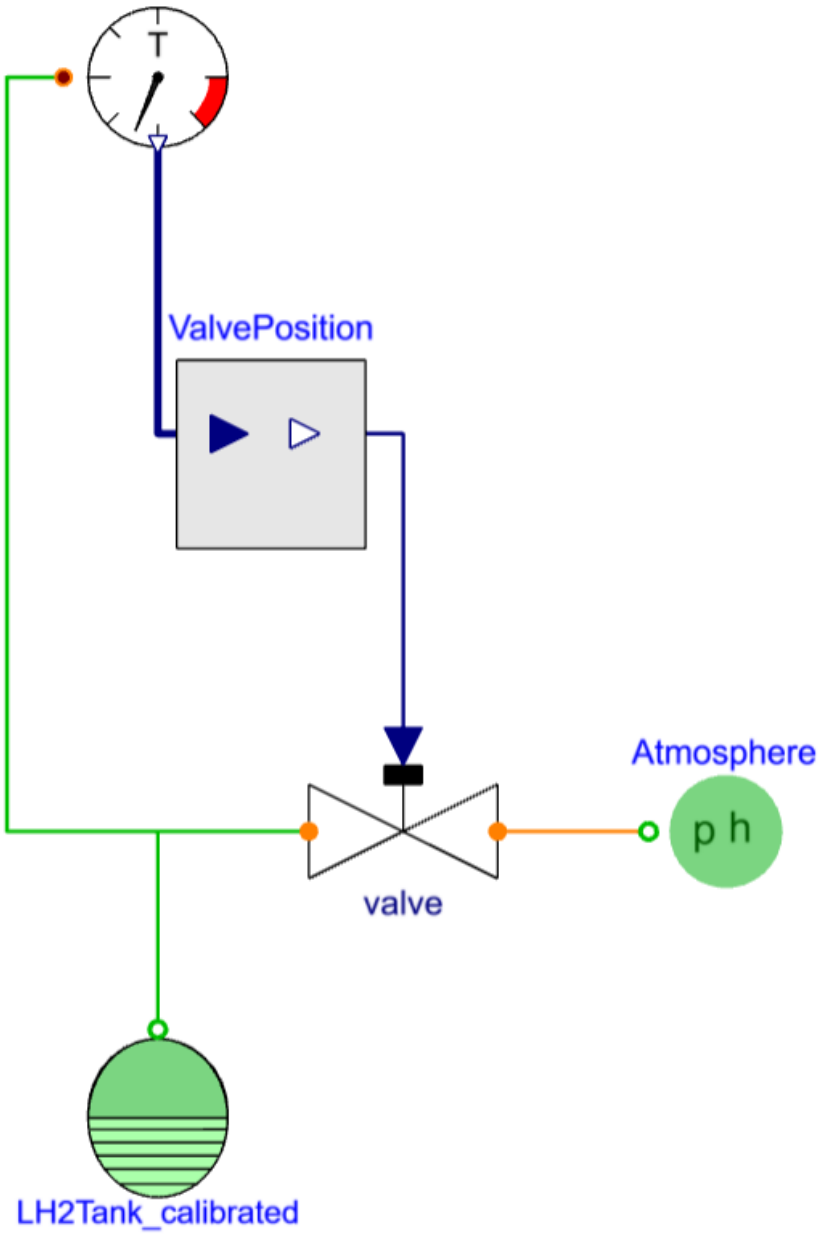

Figure 4.1 – Graphical depiction of simulation of Steady boil-off conditions in Modelon Impact. The storage tank is named LH2Tankcalibrated. When the vapor temperature (measured by the temperature sensor) reaches 35 K, then a custom component *ValvePosition* changes the input state to the valve from being fully opened to fully closed. *Atmosphere* defines the back pressure (1 atm).

Due to the lack of reported information regarding the insulation system used, the free convection model was not employed in the simulation and overall heat transfer coefficients U_{liq} and U_{vap} were instead calibrated for the liquid and vapor phase, respectively. Additionally, the dynamic wall model was not employed and instead wall temperatures were set to have constant values throughout the simulation . The data used for model calibration was from the isothermal experiment, with the intention of using the steady boil-off for validation. Since the heat transfer coefficients should not noticeably change when simulating using different initial conditions, the hope was that model parameters obtained from one experiment could be utilized to simulate the dynamics of the other.

4.1.1 Parameter calibration

The overall heat transfer coefficients to be calibrated were defined as to describe the total heat transfer into each control volume in contact with the tank wall:

$$\begin{aligned} \dot{Q}_{WL,i} &= U_{liq} A_{WL,i} (T_{external} - T_{LB,i}) \\ \dot{Q}_{WV} &= U_{vap} A_{WV} (T_{external} - T_v) \end{aligned} \tag{4.1}$$

$T_{external}$ is the ambient temperature outside of the tank sourced from [3]. Notice that there is only one value of U_{liq} shared amongst all liquid boundary control volumes. Besides the wall heat transfer coefficients, it was also decided to calibrate the heat transfer coefficient α_{cond} for the interface heat transfer presented in section 3.1.2 for both the liquid and vapor side of the interface. This was done to achieve an overall better match to the experimental data.

Case 1: Temperature Calibration

To begin with, only the average vapor temperature T_v reported by Hasan et al. [3] was taken into account when calibrating. The calibration was performed using the gradient-free Nelder-Mead simplex algorithm, and the objective function to be minimized was defined as a sum-of-least-square:

$$f^{obj}(x) = \sum_{i=1}^{M} \left(T_v^{sim}(t_i, x) - T_v^{meas}(t_i) \right)^2 \tag{4.2}$$

where t_i $(i = 1, 2, \ldots, M)$ are the time points for the measured data and T_v^{meas} and T_v^{sim} are the measured and simulated data points, respectively.

The reason the Nelder-Mead simplex optimization algorithm was chosen for the calibration was mainly because it require no jacobian evaluations to find local minimum objective function values. For more information on the Nelder-Mead algorithm the reader is referred to [37].

The resulting temperature profile for the vapor can be seen in Figure 4.2, where the simulation was able to get reasonably close to the experimental data when using optimal parameters. Additionally, Figure 4.3 shows how the temperature distribution along the height of the storage tank also seems to agree with the data. According to Figure 4.3b the experimental temperature distribution of the bulk liquid is more or less uniform along the entirety of the submerged portion of the tank, with a slight showing of stratification very close to the interface only after a long time. This homogeneous profile was captured by the simulation along the tank, as all bulk liquid control volumes had approximately the same temperature. The stratification effect close to the interface were captured to some extent by the simulation, mainly as a consequence of the temperature distribution introduced by the geometric grid. However, the stratification was not as pronounced as suggested by the experimental data.

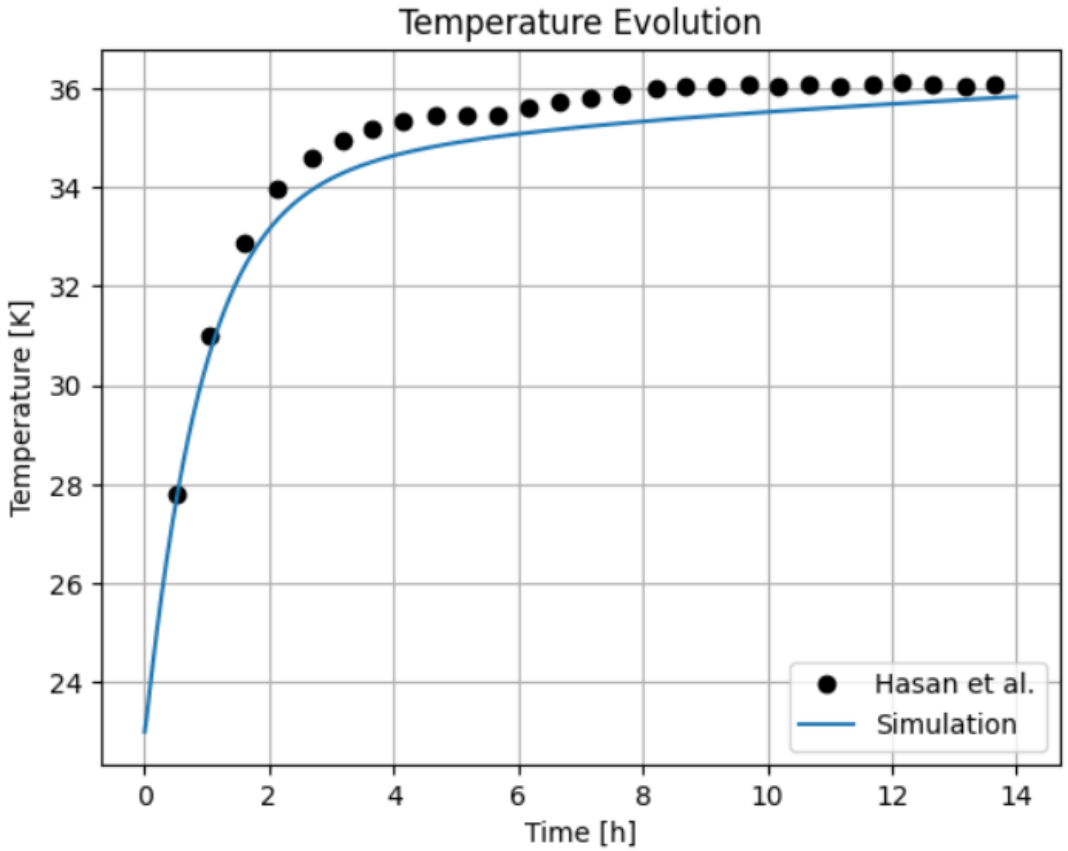

Figure 4.2 – Simulated vapor temperature profile inside the tank using calibrated parameters compared to experimental values.

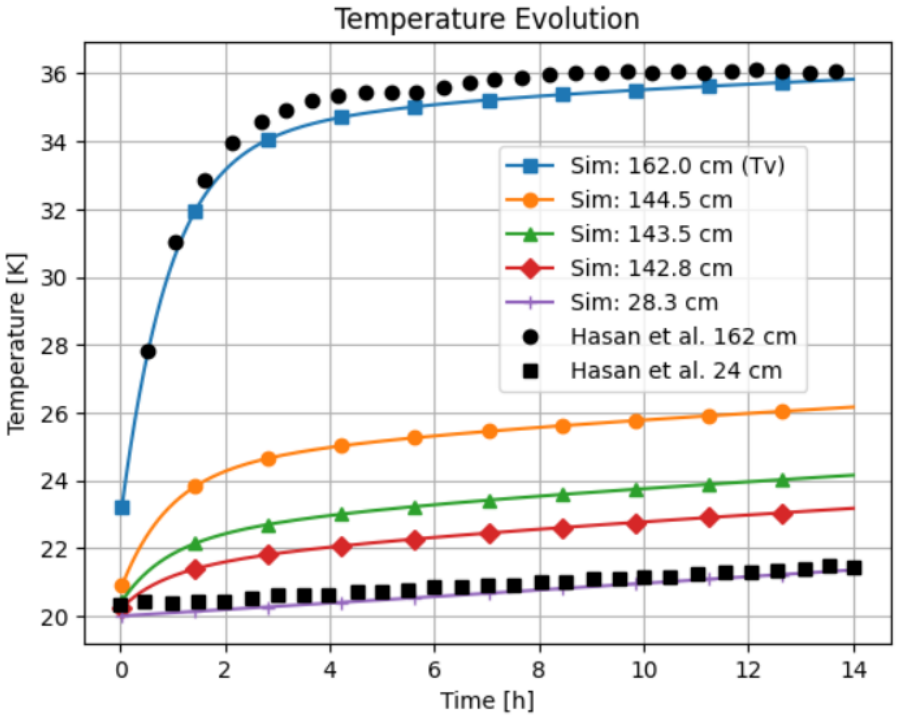

(a)

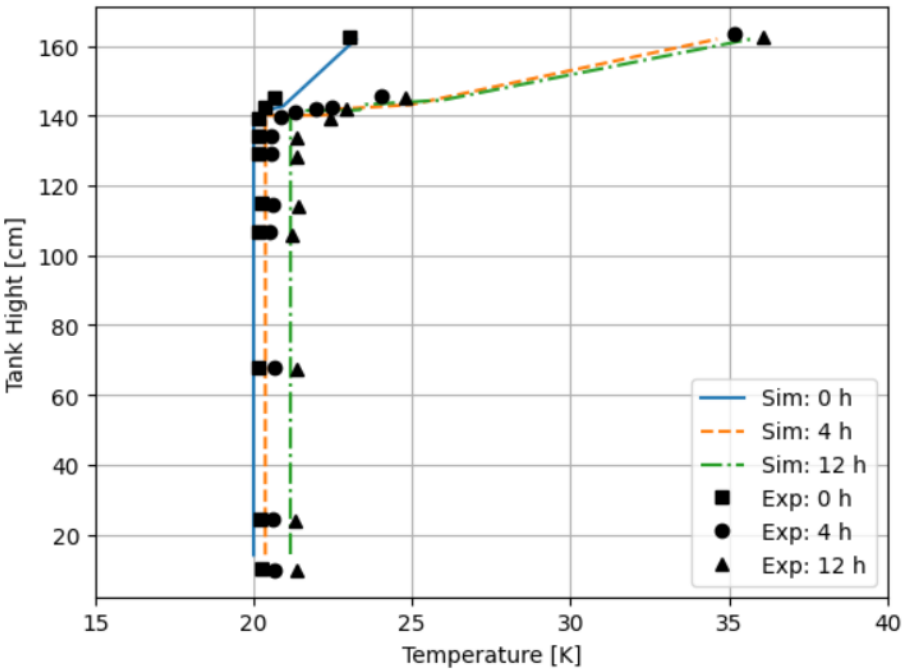

(b)

Figure 4.3 – (a) Simulated temperature evolution over time inside storage tank at different tank heights. (b) Temperature profile along height of storage tank at three different time instances compared to experimental data. The interface is situated at approximately 140 cm.

Unfortunately, the simulated pressure inside the tank was overestimated by a significant amount when using the parameter values calibrated only with respect to temperature, which can be seen in Figure 4.4. These results are disappointing, however, not entirely unexpected when considering that the parameters that affect the heat flow to and from the interface (α_{cond}) are of less significance as far as vapor temperature is concerned (which is the basis for the calibration). They are, however, intrinsically tied to the temperature of the interface, which in turn is tied to the pressure. Therefore, there is likely many trivial combinations of parameter values that result in a good fit for temperature, but only a limited number of values that could produce a good fit for both temperature and pressure.

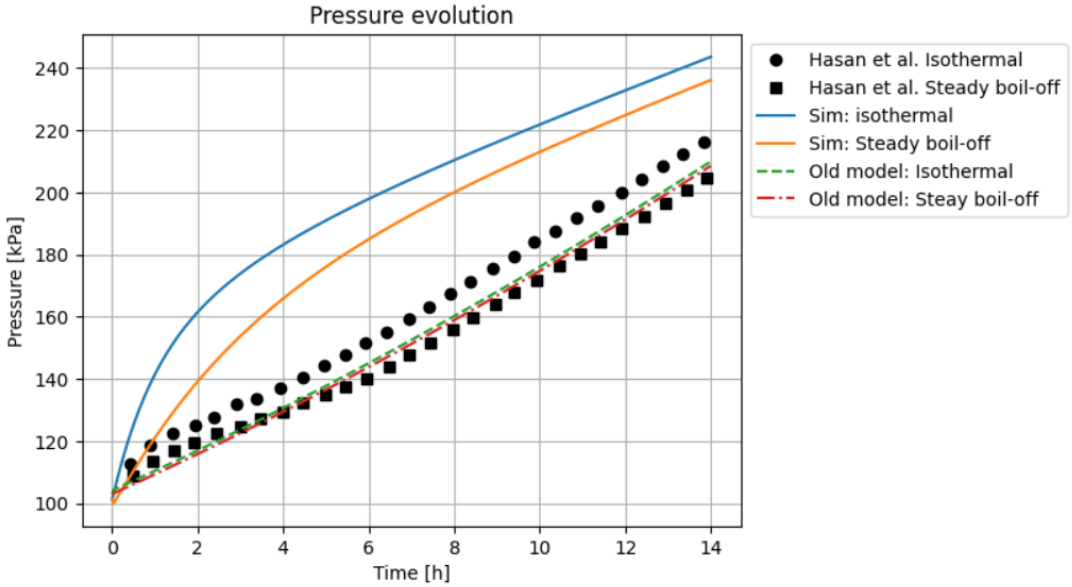

Figure 4.4 – Simulated pressure evolution after calibration only with respect to vapor temperature T_s compared to experimental data. Simulation results from the old model are also included.

Case 2: Temperature and Pressure Calibration

Now the model was calibrated using both temperature and pressure data. The pressure was taken from the isothermal self-pressurization experiment performed by Hasan et al. Including additional pressure data points for calibration of the model can easily be done by simply extending the objective function with the relevant terms:

$$f^{obj}(x) = \sum_{i=1}^{M} \left(T_v^{sim}(t_i, x) - T_v^{meas}(t_i)\right)^2 + \sum_{i=1}^{M} \left(p^{sim}(t_i, x) - p^{meas}(t_i)\right)^2 \tag{4.3}$$

The optimal values of all parameters according to the calibration in both Cases 1 and 2 are summerized in Table 4.1

Table 4.1 – Parameter values obtained via calibration with experimental data. Case 1) Only with respect to T_v. Case 2) Using both temperature and pressure data.

Parameter calibration summery				
Parameters [W/(m$^2 \cdot K$)] :	U_{liq}	U_{vap}	$\alpha_{cond,LS}$	$\alpha_{cond,VS}$
Case 1:	0.015	0.028	600	128
Case 2:	0.040	0.030	3615	120

Figure 4.5 shows the resulting pressure profile after calibration. The isothermal simulation is now very close to the experimental data, where even the initial transient behavior is captured quite adequately. Meanwhile, the steady boil-off simulation follows the measured data to some extent initially. However, constant pressure-rise rate is obtained only 2 h after closing the vent, leading to a consistent overestimation of the pressure of approximately 10 kPa in the tank. In this regard the old model is seemingly more accurate then the new one. Drawing definitive conclusions regarding these observations would of course be premature, as there as several factors that could play a role in the steady boil-off validation being off. One such factor is the difficulties of recreating the exact same operating conditions used to arrive at steady boil-off in the same manner done experimentally.

Temperature evolution in different parts of the tank can be seen in Figure 4.6. The vapor temperature is still in good agreement with experimental data after calibration, as can be seen in Figure 4.6a. However, it is evident that the temperature in the liquid domain is now overestimated when compared to what was observed experimentally (especially prominent in Figure 4.6b). A potential reason for this can be explained by looking at the values of the calibrated parameters in Table 4.1, as it is mainly the parameters associated with the liquid phase (U_{liq} and $\alpha_{cond,L}$) that

are noticeably different between the two cases. A higher value of the heat transfer coefficients will ultimately result in an overall larger heat transfer into the liquid domain, which explains the apparent temperature increase.

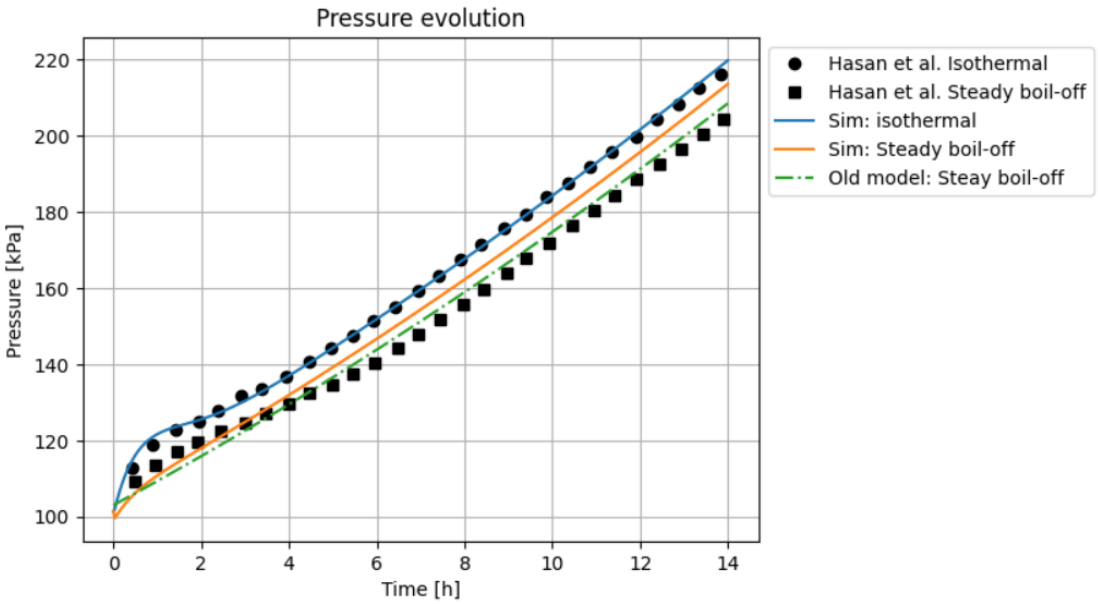

Figure 4.5 – Simulated pressure evolution after calibration with respect to both vapor temperature and isothermal pressure data.

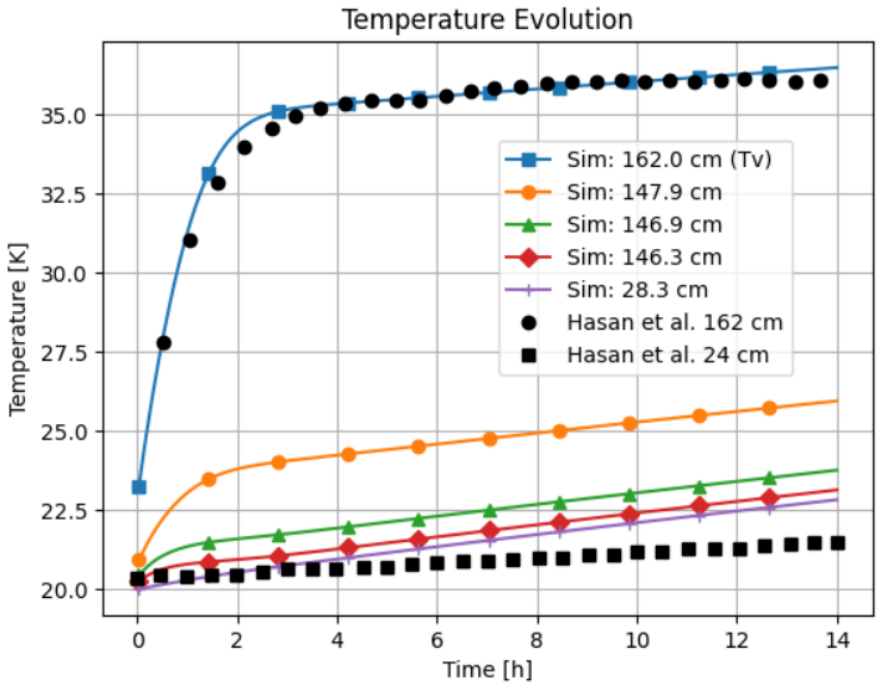

(a)

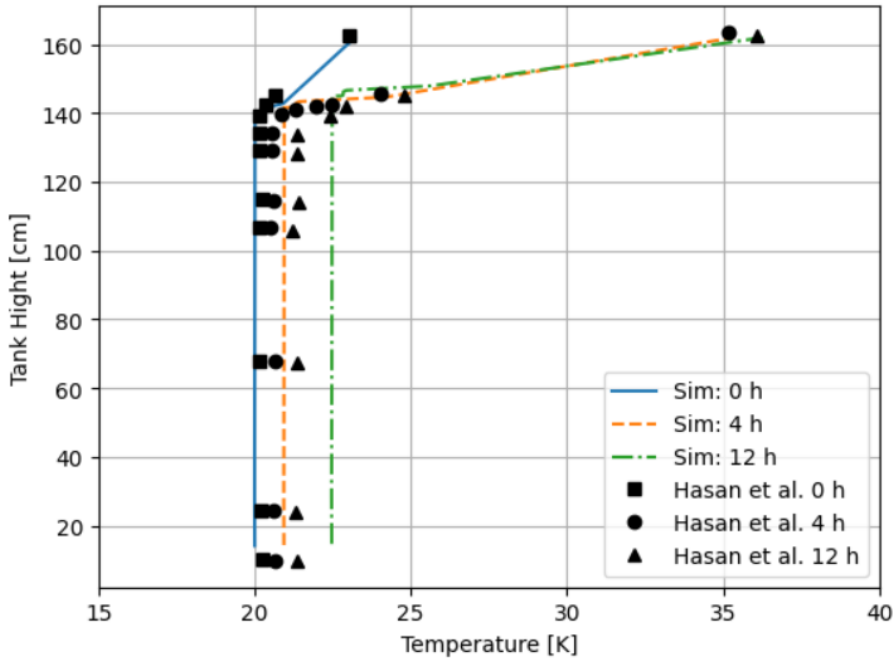

(b)

Figure 4.6 – Temperature profiles when calibrating with respect to both temperature and pressure. (a) Simulated temperature evolution over time inside storage tank at different tank heights. (b) Temperature profile along height of storage tank at three different time instances compared to experimental data. The interface is situated at approximately 140 cm.

The average heat flux calculated over the course of the Case 2 simulation was 7.57 W/m^2, more than twice the amount estimated for the actual process by Hasan et al. This could be an indication that the calibrated overall heat transfer coefficient for the liquid is overestimated, and that perhaps some other combination of parameter values could result in a better overall fit with respect to liquid temperature while still matching vapor temperature and pressure data. For example, a slightly smaller U_{liq} coupled with a larger $\alpha_{cond,LS}$ might result in only the liquid temperature being different, while keeping the other states more or less unchanged. This is of course mainly speculation, and would require a new calibration where liquid temperature is included as a reference.

One interesting observation can be made by comparing the calibrated values of α_{cond} with what they would have been if one had just used the original expression derived in Section 3.1.2 (eq 3.45):

$$\alpha_{cond} = \frac{\kappa}{h_0} = \sqrt{\frac{\kappa \rho C_p}{\tau}}$$

The values of α_{cond} throughout the simulation together with their average values can be seen in Figure 4.7. It is clear that the calibrated parameters are larger, with the coefficients for liquid and vapor being 320% and 83% bigger than the average values, respectively. Since eq 3.45 is based on the assumption that heat transfer at the interface is due to only thermal conduction, the discrepancy in values could indicate that this assumption is fallacious and that there is also a fare bit of convection, especially on the liquid side. This realization is actually well backed by theory, as the whole concept of thermal stratification is fundamentally a phenomenon stemming from convective liquid flow accumulating stratified mass at the surface (see Section 2.1.3).

Since the Nusselt number is defined as the ratio between convective and conductive heat transfer, one could argue that (provided that the calibrated parameter value is trustworthy) the ratio between the calibrated and average heat transfer coefficient approximates the average Nusselt number. The expression in eq 3.45 could then be

revised as:

$$\alpha_{cond} = \frac{\kappa}{h_0}\overline{Nu} = \frac{\kappa}{h_0}\begin{cases} 4.2, & \text{if liquid} \\ 1.83, & \text{if vapor} \end{cases}$$

The above correlation would of course only be applicable to this particular case, and the Nusselt number would still need to be calibrated for other tank geometries and operating conditions. At that point one might just as well continue calibrating the entire heat transfer coefficient.

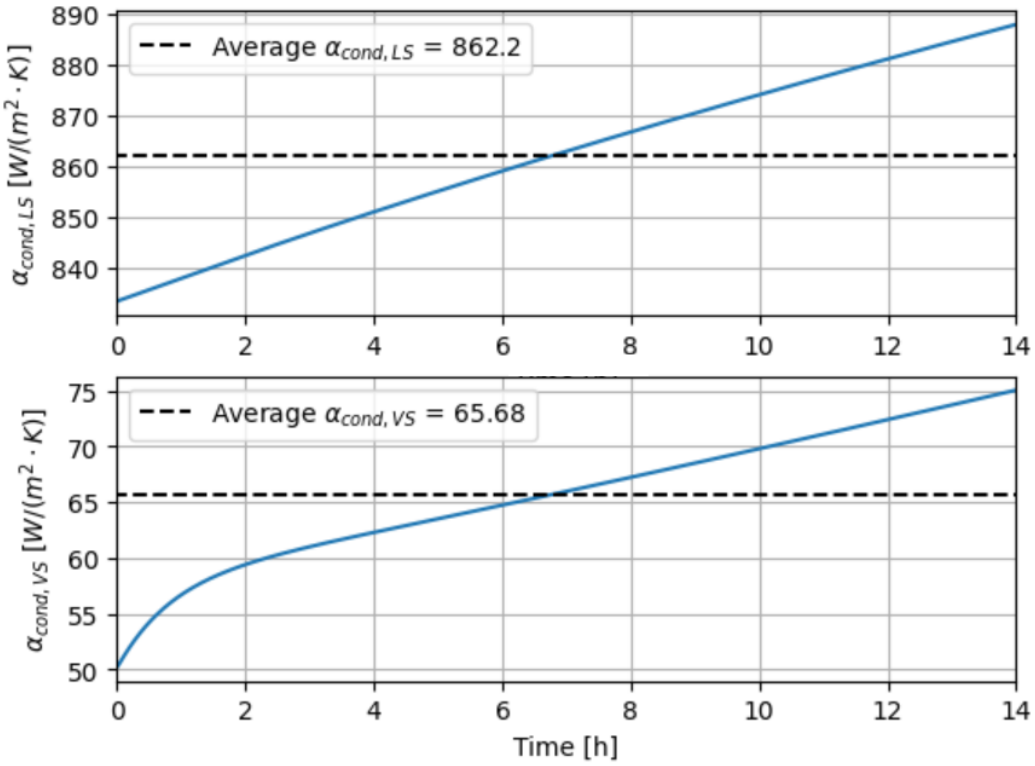

Figure 4.7 – Range of values for α_{cond} during the simulation for both phases when using the expression derived in section 3.1.2. The average values are significantly smaller than the calibrated ones (Case 2).

4.1.2 General comments on calibration

The model could produce results that were in overall good agreement with experimental data when optimal parameters where employed (here referring mainly to

Case 2). This may seem like a redundant statement since calibration entails finding values that result in the best possible fit, but there is never any guarantee a combination of parameter values exist that produce a "good" fit. The fact that the model could predict both vapor temperature and pressure to such a degree still speaks to its ability to depict the underlying physical phenomena that gives rise to these profiles. This is especially noteworthy for the initial isothermal pressure rise rate, which could not be captured by the old model even when calibration was used.

The observed deviations in liquid temperature could be a result of a non-optimal combination of calibrated parameter values, as mentioned earlier; however, it could just as well be because of inherent issues or limitations with the model. One assumption that could introduce potential errors in this case was that the wet wall temperature was set to a constant value of 30 K during the simulation. The reason behind it having such a high value relative to the liquid bulk was to avoid numeric complications arising when these two values become the same. This is a persisting robustness issue with the model that has yet to be fully resolved. A high wall temperature does not affect the heat transfer into the tank in this case since these were calibrated for, however, it does influence the convective flow profile of the liquid boundary layer close to the wall. A large temperature gradient will result in a large vertical flow, which could in turn affect the temperature evolution in the tank.

Finally, it is important to remember that the outputs of any model can only be as good as the inputs that are fed to it. There could always be inaccuracies inherent in the experimental data, and recreating the exact experimental setup in a simulation can be a daunting task when only limited information is available.

4.2 Various studies

After validation had been performed it was decided to use the developed model to simulate a couple of different storage scenarios. The following section is primarily meant to showcase some of the capabilities and features of the model, and will therefore not focus too strongly on in-dept analysis of the simulation results.

4.2.1 Study 1: Long term storage

Since one important purpose of the storage tank is to hold liquid hydrogen for extended periods of time, an obvious scenario would be to use the model to simulate long term storage conditions. In this test, a medium sized tank was exposed to nothing but ambient heat flux for several days to investigate the effects of thermal stratification and self-pressurization within the storage tank.

The tank was modeled as a horizontally oriented cylinder with flat ends. The internal length and radius were set to 20 m and 4 m, respectively, equating to a total storage capacity of about 1000 m^3. The dynamic wall model was employed so as to have a non-constant wall temperature throughout the simulation. The tank wall material, for the sake of simplicity, was assumed to consist of a 100 mm thick layer of pure Mylar polyester film without the inclusion of vacuum jackets. The properties of the wall are listed in Table 4.2 and were taken from [38].

Table 4.2 – Summary of wall properties used to model the tank wall/insulation system during the simulation.

Wall properties				
Material	C_p $[J/(kg,K)]$	ρ $[kg/m^3]$	κ $[W/(m,K)]$	Thickness [mm]
Mylar:	1172.3	1390	0.1549	100

The tank had an initial fill level of 60%, meaning the mass of liquid hydrogen was just under 45 metric tonnes. It was assumed that all liquid hydrogen had a slightly sub-cooled homogeneous temperature of 20 K at the start of the simulation (at atmospheric pressure). Likewise, the vapor temperature was set to be slightly overheated at 23 K. Both the wet and dry walls were assumed to be slightly hotter than their respective fluid phase initially. The external temperature was assumed to have a constant value of 298 K. Like in the previous section, the liquid domain was divided into 10 horizontal control volumes and the fluid close to the interface was discretized into 3 cells on each side. The simulation spanned a period of around 111 hours, or 4.6 days.

Pressure and Temperature

Figures 4.8 and 4.9 show the pressure evolution and vapor temperature inside the storage tank. It is clear that the initial pressure transient has the familiar appearance of the experimental data presented in the validation section. However, in this case it is likely due to the very rapid heating of the vapor phase by the already hot dry wall as shown in Figure 4.9. As soon as the vapor and wall temperatures are close to one another in value we see an immediate reduction in pressurization lift, followed by a slow stabilization period that transitions into a constant pressure rise rate after approximately 20 hours. Similar dynamics are observed for the vapor temperature.

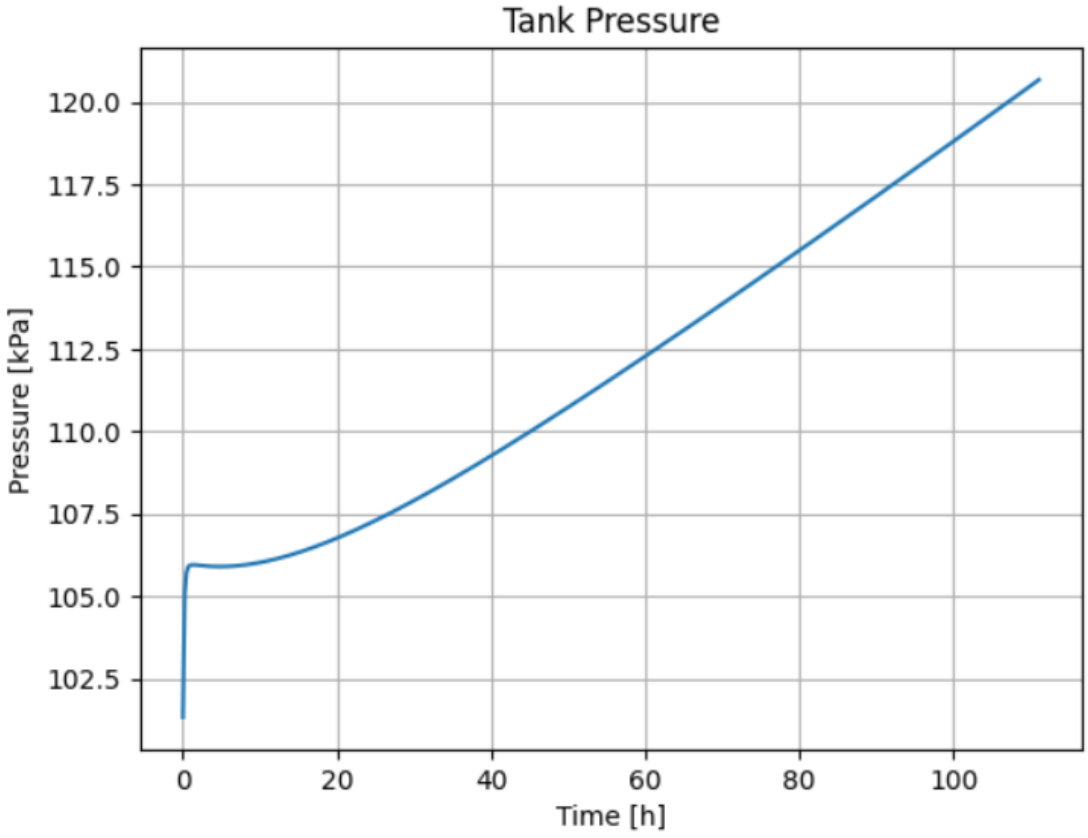

Figure 4.8 – Pressure evolution inside the storage tank over time. The initial tank pressure was 101 kPa (1 atm).

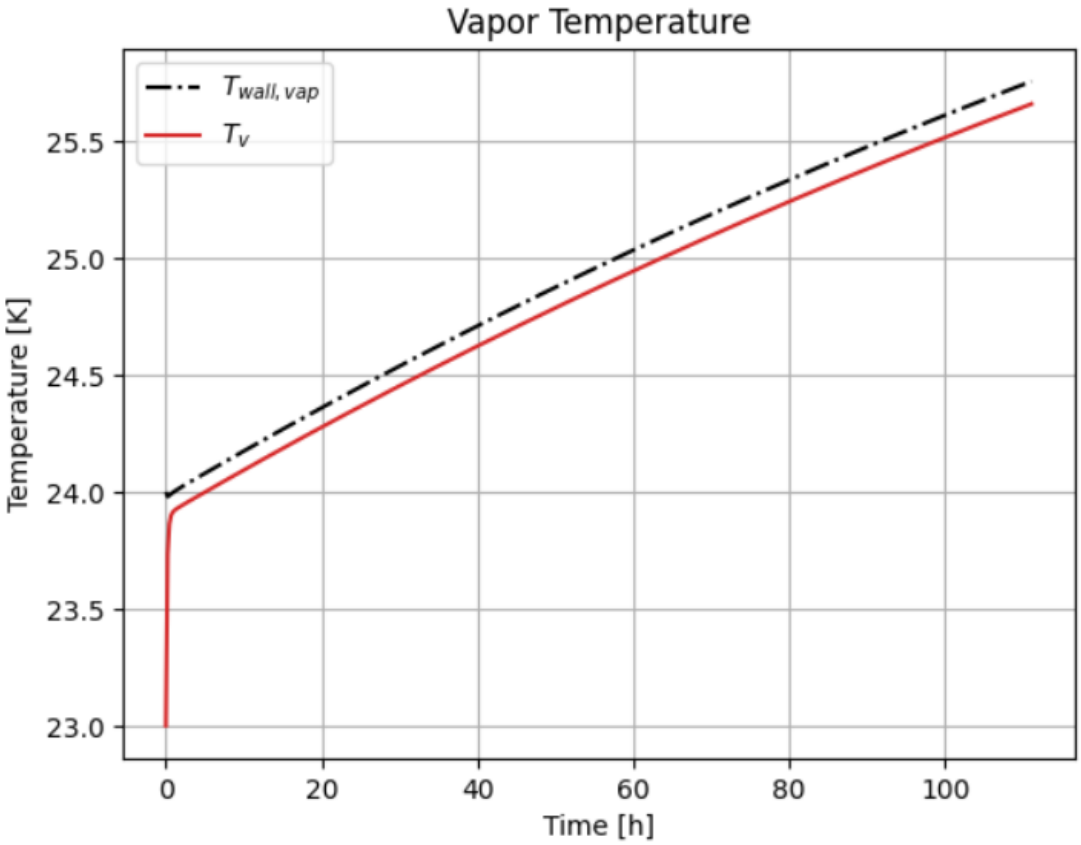

Figure 4.9 – Temperature evolution of the vapor phase together with the temperature of the dry wall throughout the simulation.

Thermal stratification

Figure 4.10 shows that there is a small temperature gradient present in the liquid bulk along the tank height very shortly after beginning the simulation (within the first hour). However, the remainder of the time the bulk liquid is more or less uniform, with the exception of liquid close to the interface. The same thing can also be seen in Figure 4.11, where it is shown that the wet wall is rapidly cooled by the liquid until an almost constant temperature difference is reached. Overall, the liquid temperature is only increased by about 0.6 K during the entirety of the simulation.

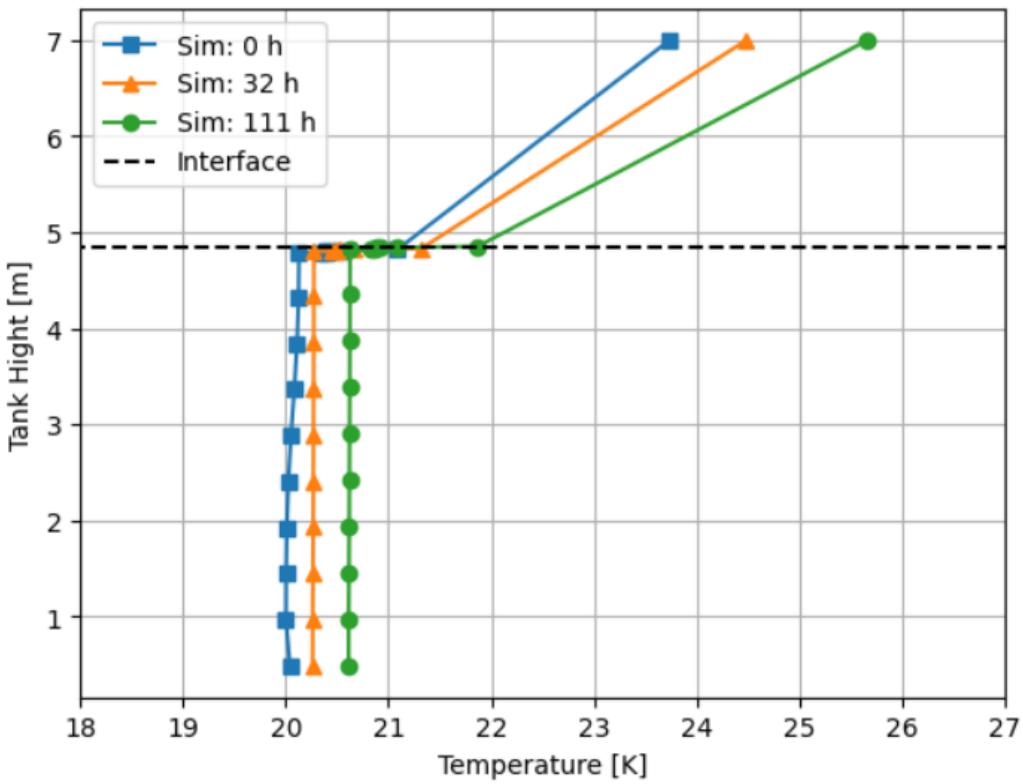

Figure 4.10 – Temperature profile along the height of the tank at three different time instances.

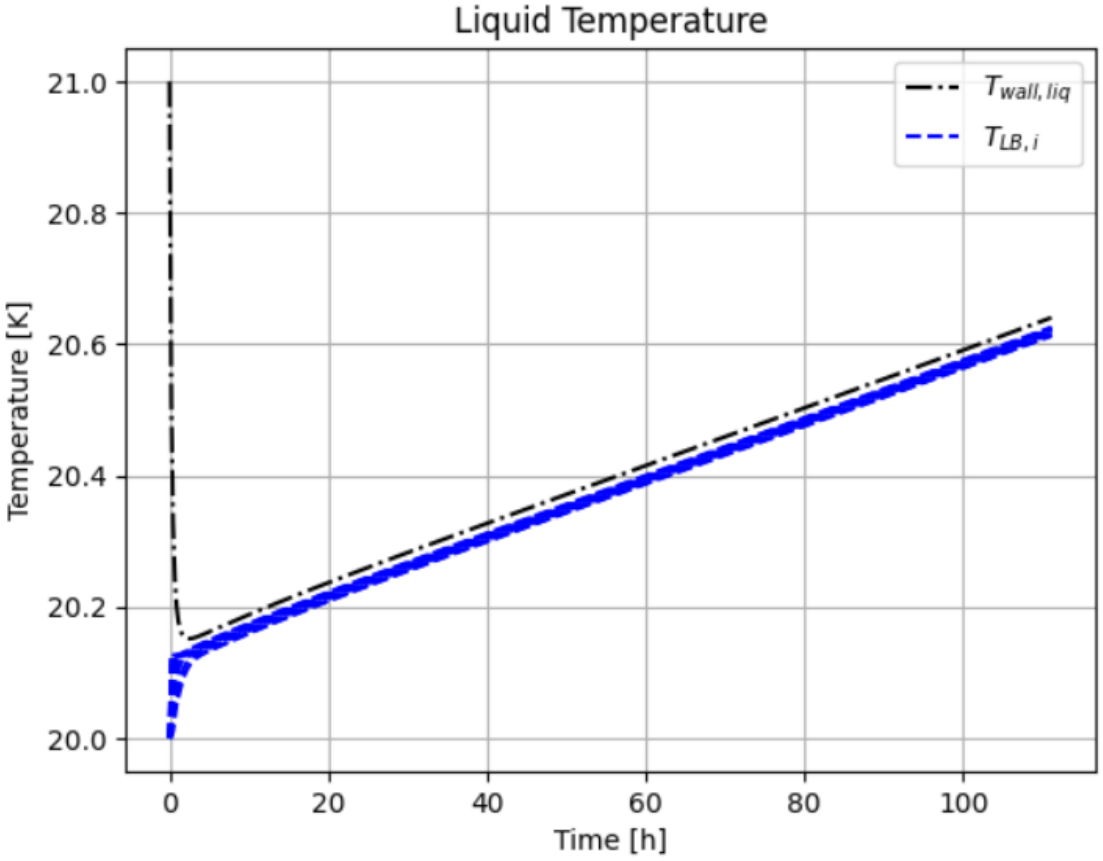

Figure 4.11 – Temperature of all liquid bulk elements together with the temperature of the wet tank wall throughout the simulation.

Figure 4.12 shows a close up view of the liquid control volume temperatures after only a short time of simulation. As expected, the boundary layer control volumes are heated more rapidly than the bulk. However, the temperature difference is still very small, way within the margin of error for most temperature sensors. It is also evident that all control volumes becomes more or less homogeneous in temperature after only three or so hours.

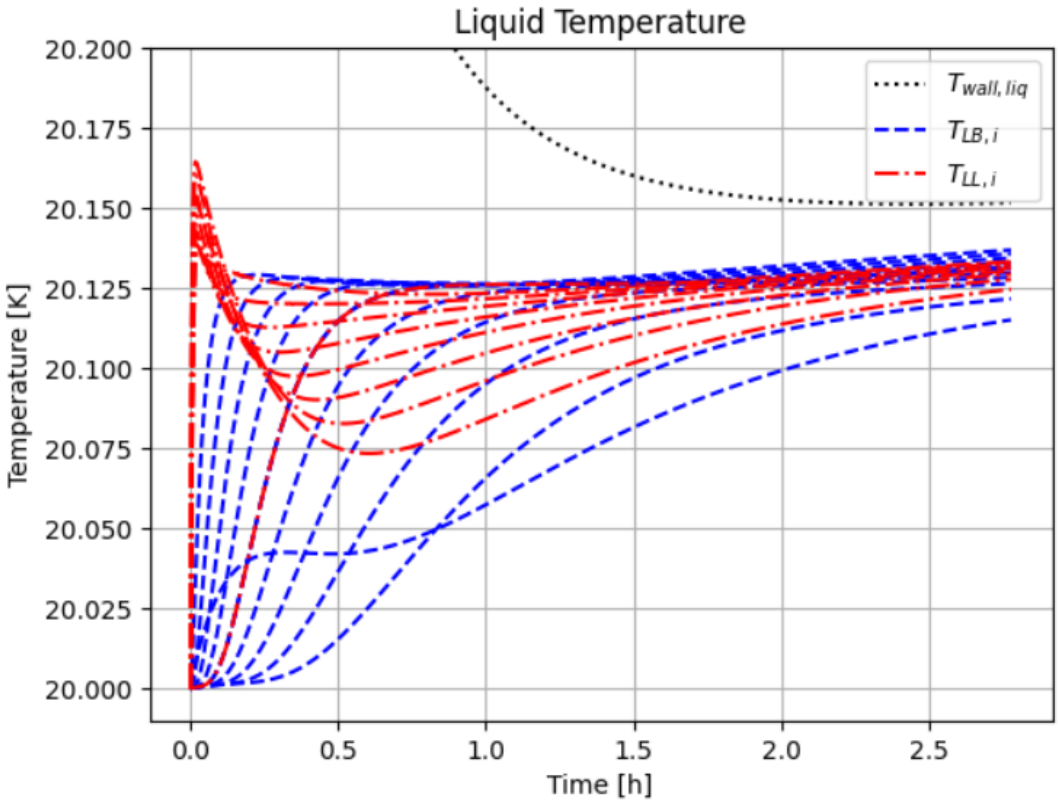

Figure 4.12 – Temperature distribution of the liquid domain after a short period of time. This graph is essentially a zoomed in version of 4.11

Figure 4.13 shows the size of the developing boundary layer close to the tank wall over time. Most of the growth of the boundary layer occurs within the first few hours of the simulation, after which it reaches a constant thickness. This makes sense when considering the temperature difference between the liquid and the tank wall also stays at an almost constant value after some time as seen in Figure 4.11. Remember that the empirical correlation used to estimate the boundary layer thickness contains the Grashof number, which in turn is dependent on the temperature gradient (see eq 3.8).

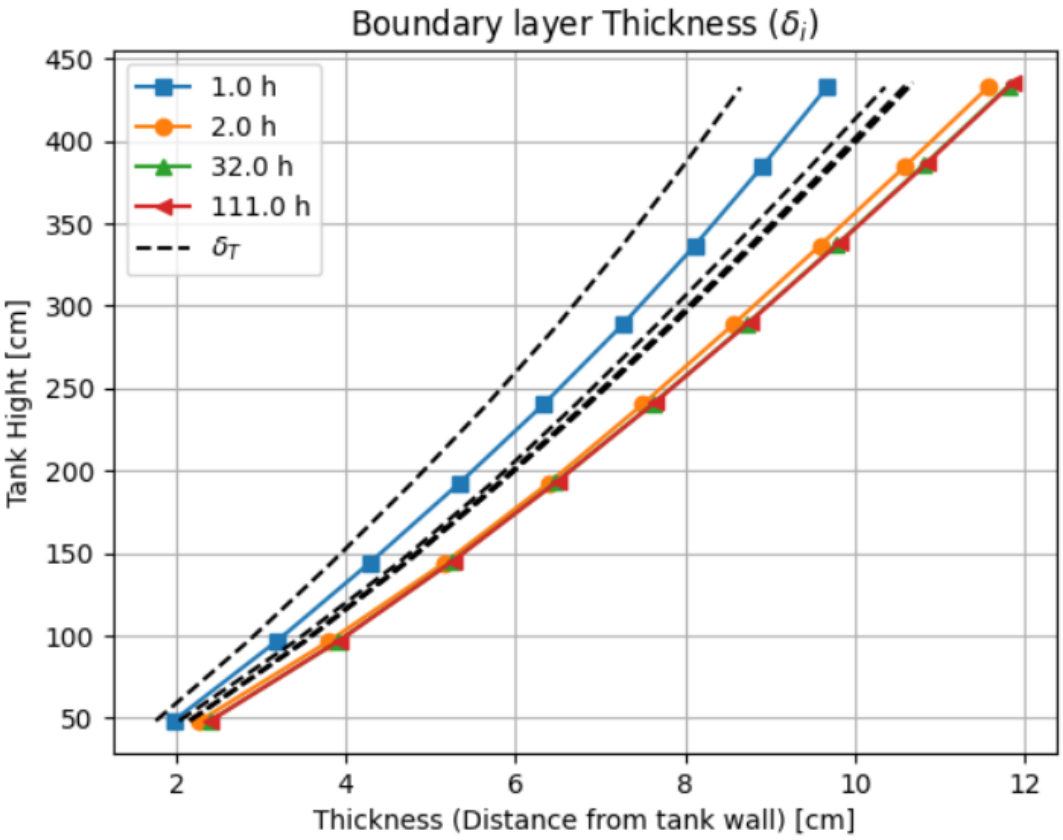

Figure 4.13 – Development of the velocity boundary layer close to the wet tank wall over time. The thermal boundary layer δ_T is depicted by the black dashed lines.

Velocity Field

One interesting aspect of the model is that it uses empirically derived correlations to represent the convective flow close to the wet walls of the tank. This makes it possible to investigate the characteristics of the approximate "flow field" within the liquid domain. Figures 4.14 and 4.15 show the velocity profiles close to the wall and between the bulk elements, respectively.

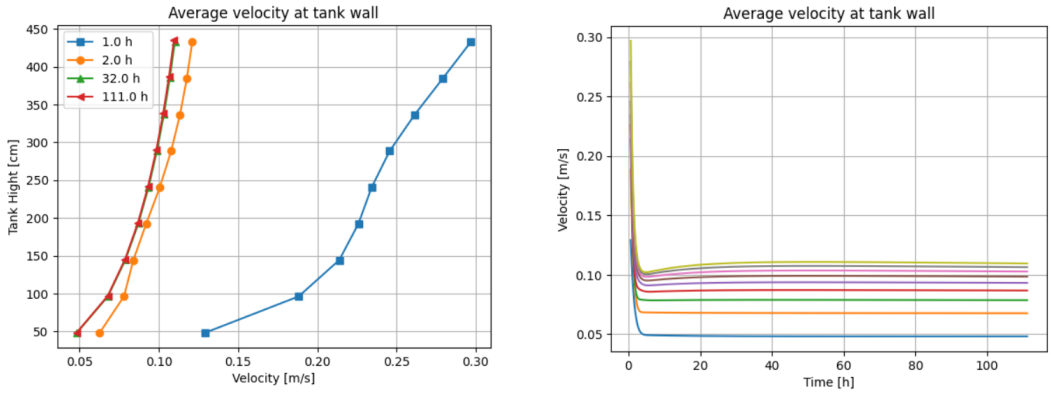

(a) Velocity profile along height of tank. **(b)** Velocity profile over time.

Figure 4.14 – Average velocity next to the tank wall in the boundary layer subdomain a) along tank height, and b) with respect to time.

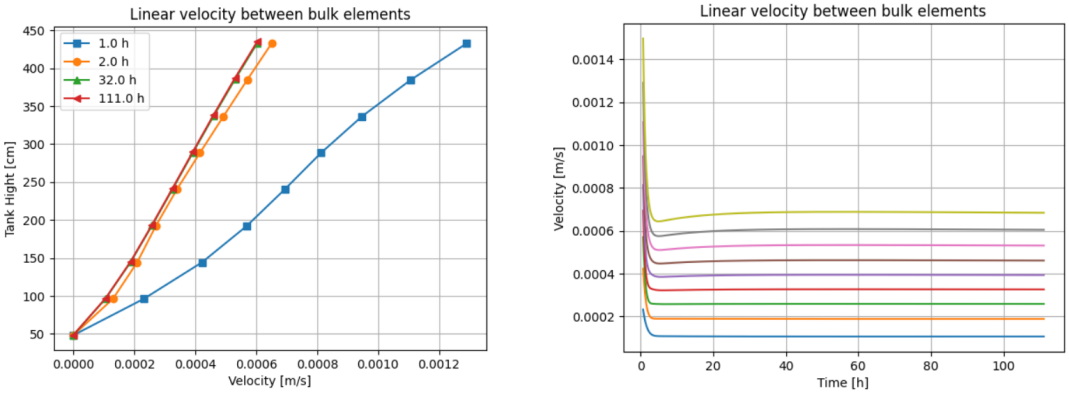

(a) Velocity profile along height of tank. **(b)** Velocity profile over time.

Figure 4.15 – Linear velocity in the bulk liquid a) along tank height, and b) with respect to time.

The velocity at the walls is several orders of magnitude larger than in the liquid bulk. This is of course expected from theory, as described in Section 2.1.3. Remember that the flow next to the wall is defined to have a positive direction towards the interface, while the bulk flow is defined using the opposite convention (see Figure 3.1). Figure 4.14a clearly shows that, after an initial transient, the velocity profile at the tank wall takes the familiar shape presented in Figure 3.3. One needs to keep in mind that the correlations used to estimating the velocity are based on experimentally observed profiles for flat vertical plates. In the model it is assumed that these correlations are still valid at other tank wall geometries, which is most likely not the case. If these velocities are representative of the actual flow field in the real process is impossible

to answer without a thorough comparison to experimental data, however, the fact that it can be modeled in this way can still give valuable insight into the dynamical behavior of the tank content.

Boil-off

The mass and heat exchange between the gas and liquid phase in the storage tank is summarized in Figure 4.16.

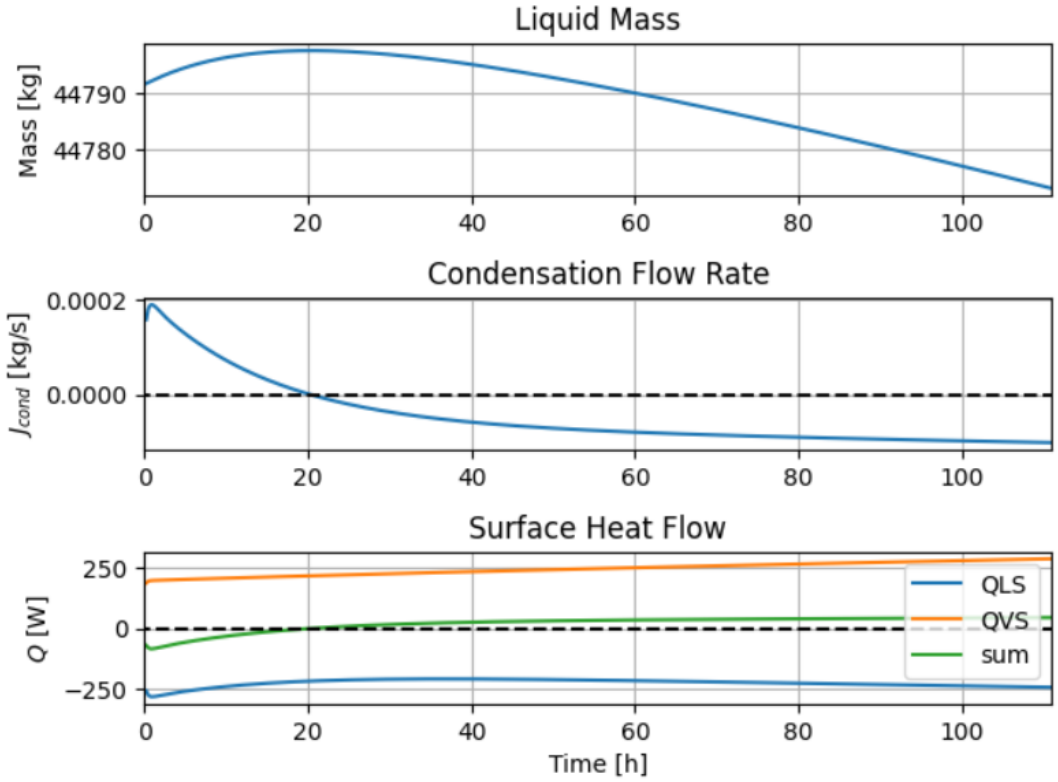

Figure 4.16 – Parameters pertaining to mass and energy exchange between the gas and liquid phase with respect to time.

Initially there is a net positive condensation flow in the tank leading to an increase in overall liquid mass. However, after around 20 h evaporation takes over and the mass begins to decrease for the remainder of the simulation. The two bottom graphs essentially show the same thing: the point at which the evaporation flow rate is greater than condensation. For a closed system where no mass either enters or leaves the tank J_{cond} will be equal to the time derivative of the whole liquid

domain. J_{cond} is dependent on the sum of heat transfer flow rates to the interface from the two phases, as derived in eq 3.47. Of course, had there been liquid boiling at the tank walls then J_{cond} would not have been the only mass flow to and from the liquid domain since bulk evaporation would have been accounted for as described in Section 3.5. However, this never happened during the simulation.

Even longer storage time

Finally, the same tank presented above was simulated for an even longer period of time – a total of 46 days – to see how values like pressure, temperature and boil-off would develop. The results of the simulation show that the vapor temperature eventually approach some steady-state value around 30 K, as can be seen in Figure 4.17a. The pressure keeps on increasing at about the same rate until the end of the simulation, with a final value of 3.5 bar. Figure 4.17b shows how the liquid mass keeps decreasing at an almost constant boil-off rate of 0.21 g/s. In total, almost 670 kg of liquid hydrogen is evaporated, much of which would likely have been vented away to the atmosphere to prevent the tank pressure from getting too high in a real process. This would represent almost 1.5% of the total fuel being lost only during storage. Factoring in that storage times can be on time scales of several months or years it is evident why there are financial incentives to reduce boil-off.

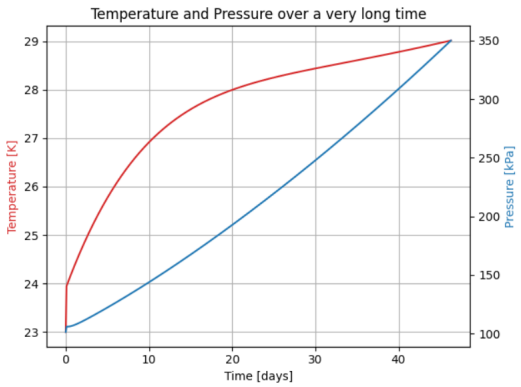

(a) Pressure and Temperature evolution with respect to time.

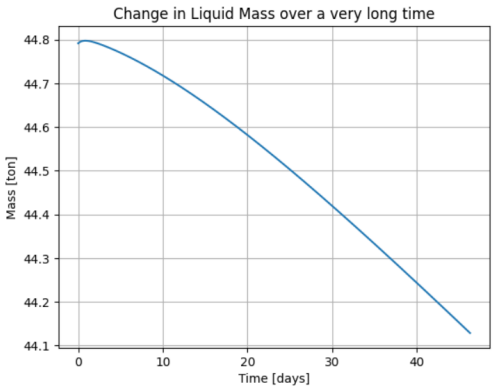

(b) Liquid mass with respect to time.

Figure 4.17 – Final temperature, pressure and mass simulation results for the long simulation.

4.2.2 Study 2: Filling of storage tank

One interesting scenario to investigate is the process of filling the storage tank with liquid hydrogen. In theory, as more and more liquid is pumped into the tank, the gas volume might become increasingly more compressed in the ullage part of the tank if not vented. This compression should cause a rapid increase in both tank pressure and temperature, something that the model ought to be able to capture.

The setup consisted of a small vertically oriented cylindrical tank with flat ends. The internal tank height was set to 5 m with an inner radius of 1 m, giving a total storage volume of 15.7 m^3. It was assumed that sub-cooled liquid hydrogen (20 K) was provided by a pump operating at $p_0 = 3$ atm of external pressure through a connecting pipe with hydraulic conductance k [kg/(Pa,s)]. The filling rate J_{fill} (same as $-J_{out}$ if Figure 3.1) was calculated through the simple equation:

$$J_{fill} = k(p_0 - p) \tag{4.4}$$

where p is the tank pressure. Filling was set to be turned off when the tank pressure reaches the external pressure. For the sake of simplicity, and because of reoccurring issues with model robustness, it was decided to not use the dynamical wall model in the simulation and instead prescribe the optimal parameters for heat transfer calibrated in Section 4.1.1. The result from running the simulation at three different values of k can be seen in Figure 4.18.

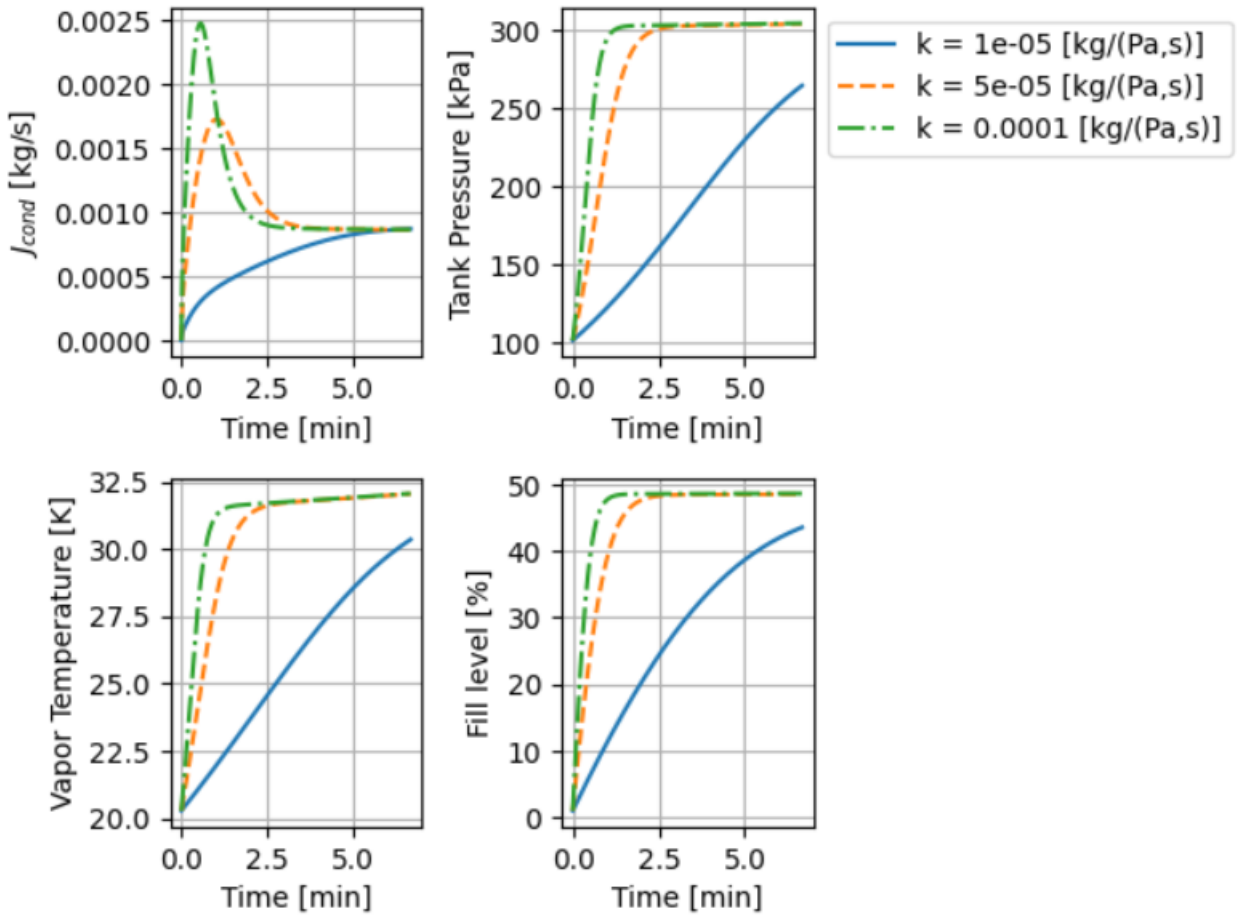

Figure 4.18 – Values of condensation flow rate, tank pressure, vapor temperature, and tank fill level over time at three different values of k.

It is evident that the speed at which the vapor pressure and temperature inside the tank increases is heavily tied to the filling rate. At the highest filling rate, the tank pressure approaches very close to the external pressure of the pump after only about 1 minute. The rapid increase in pressure and temperature is a result of the condensation flux not being able to keep up with the shrinking vapor volume, leading to gas compression. The interface temperature T_s also increases due to this compression, which inevitably leads to a larger heat transfer to the liquid phase and as such an increased evaporation rate. The evaporation rate eventually catches up with the condensation flux, leading to a prominent drop in the net condensation flow rate in Figure 4.18. This phenomenon is known as condensation blocking, and the model is able to produce similar results to other models developed to describe this process [26]. All these dynamics culminate to an effective stop in tank filling

after hitting a fill level of approximately 50%. The faster the filling rate initially, the faster this stopping point is reached. Naturally, this is a very important aspect that needs to be taken into account when performing cryogenic tank filling in practise.

4.2.3 Study 3: Different tank proportions

The final scenario was an investigation into what happens with the overall dynamics inside the storage tank as its geometrical proportions change. For this simulation, three horizontal cylindrical tanks with equal total storage volume but different aspect ratios were exposed to the same ambient conditions over a period of about 2.5 days (61 h). The aspect ratio (AR) in this context refers to the ratio between internal length L and diameter D of the tank. The exact proportions of each tank are summarized in Table 4.3. The dynamic wall model was enabled for the simulation, and the wall properties were the same as those used in Section 4.2.1. The total storage volume for all three tanks was 50 m^3 and the tanks were filled to 60% capacity at the start of the simulation.

Table 4.3 – Geometric proportions of the three storage tanks used in the simulation.

Storage Tank	Length L [m]	Radius R [m]	Aspect Ratio $\frac{L}{D}$
$\text{Tank}_{AR:1}$	4	2	1
$\text{Tank}_{AR:2.5}$	7.36	1.47	2.5
$\text{Tank}_{AR:0.25}$	1.58	3.17	0.25

The results from the simulation can be found in Figures 4.19-4.22. There is not a dramatic difference between the different tanks in regards to tank pressure and vapor temperature for most of the simulation, as seen in Figure 4.19. However, by the end there is a noticeable pressure difference of about 30 kPa between AR 0.25 and the other two tanks. A similar observation is made when looking at the liquid temperature in Figure 4.20, where AR 0.5 has a lower final temperature than the other tanks.

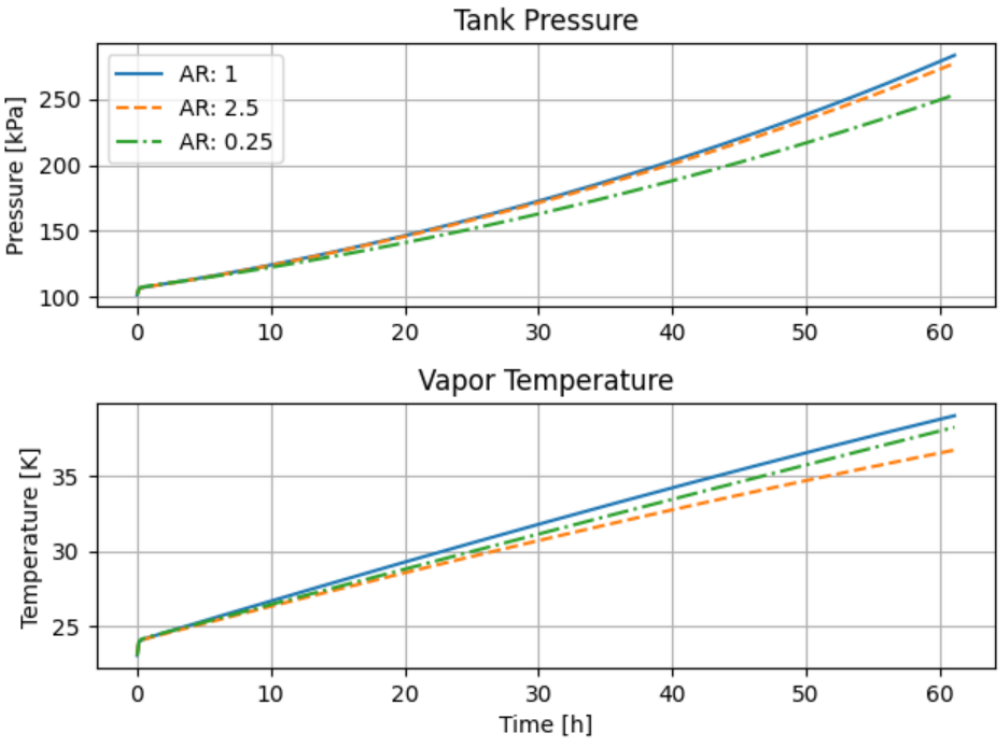

Figure 4.19 – Tank pressure and vapor temperature over time for the three different tanks.

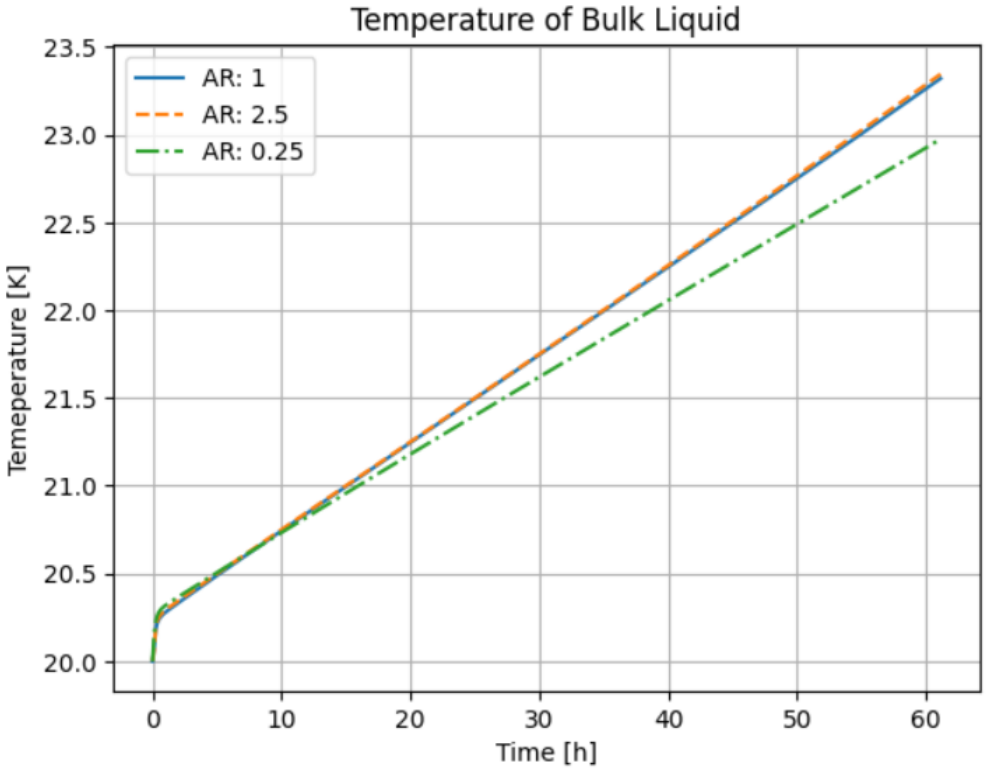

Figure 4.20 – Bulk liquid temperature inside the different tanks over time. The state values was taken from the 5:th liquid bulk element in the middle of the liquid domain.

Figure 4.21 shows how total liquid mass changes over time in the three cases, and even here it is evident that the lowest aspect ratio tank experiences an overall smaller boil-off rate than the other tanks during the course of the simulation. We can begin to explain some of these observations by considering the heat and mass transfer areas available to each tank. Table 4.4 shows that the average surface area between different parts of the tank is heavily dependent on the aspect ratio. Because of its peculiar shape, AR 0.25 actually has the largest total surface area out of all the tanks, however, most of this area comes from the tank ends. Since AR 0.25 is heated less than the others, this would suggest that heat flux through the middle section of the tank is more prominent than at the tank ends. Additionally, the liquid-to-vapor surface area (or interface area) A_{LV} for AR 0.25 is rather small. This helps explain the smaller boil-off rate observed in Figure 4.21, which also contributes to the final tank pressure not increasing as much due to self-pressurization.

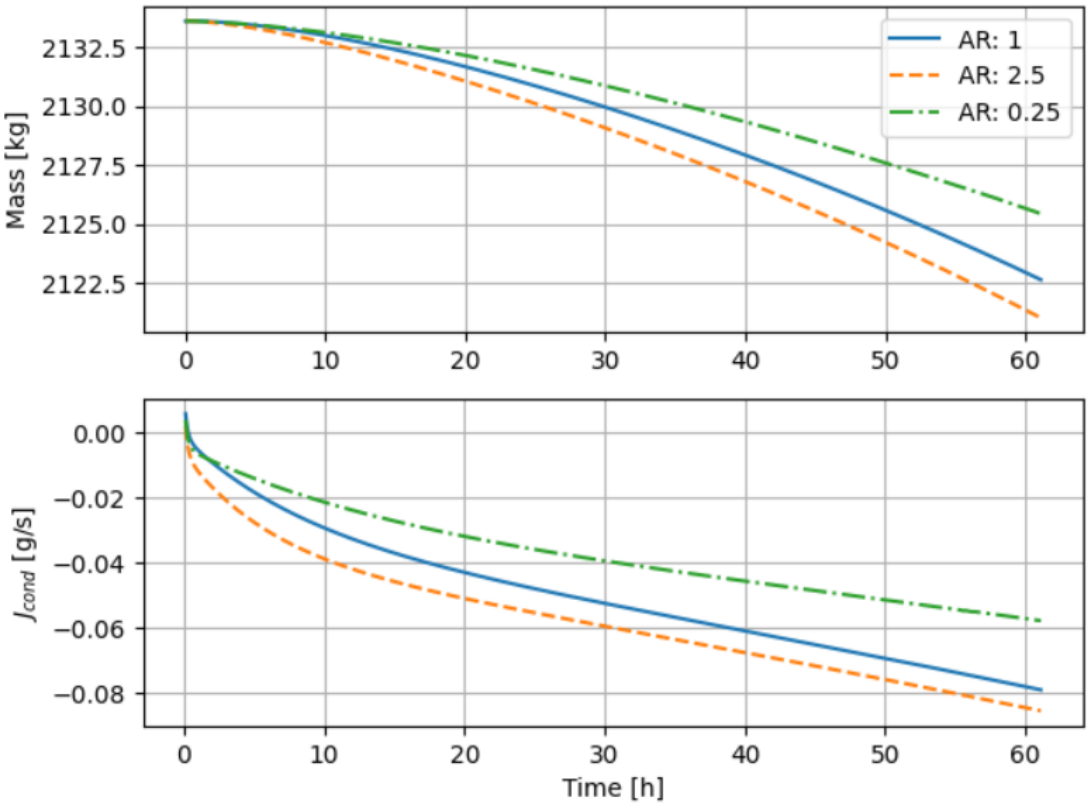

Figure 4.21 – Total liquid mass and condensation flow rate (boil-off rate) in the different tanks over time.

Table 4.4 – Average heat transfer surface areas in different parts of the tank.

Surface Areas [m^2]:	$A_{WL,tot}$	$A_{WL,mid}$	$A_{WL,ends}$	A_{LV}
Tank$_{AR:1}$	43.5	28.0	15.5	15.7
Tank$_{AR:2.5}$	46.4	38.0	8.4	21.3
Tank$_{AR:0.25}$	56.5	17.6	38.9	9.9

The average total heat transfer into the liquid domain together with the distribution of average heat transfer across the end and middle sections of the tanks can be found in Figure 4.22. The graph shows that AR 0.25 indeed experiences the least heat ingress in total. Here it is also clear that there is more heat per unit area at the cylindrical middle section in a horizontal tank than at the ends, as there is about the same amount of heat transfer at the mid section of AR 1 as there is at the end sections of AR 0.25; despite the latter having a larger heat transfer area.

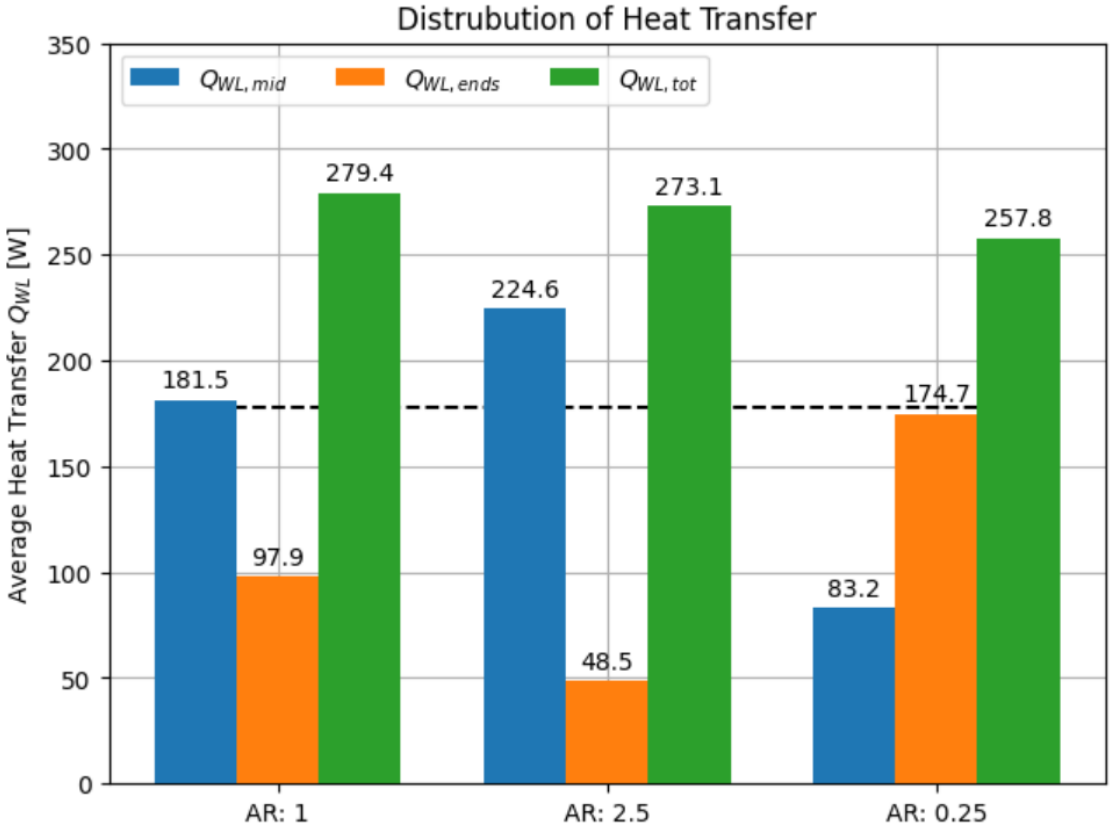

Figure 4.22 – Bar chart showing the distribution of average heat transfer across different parts of the tank as well at the total heat transfer into the liquid domain. A black dashed line has been included in the chart to show similar transfer rates between different tank sections despite a large difference in area.

The results from the simulation suggests that, for horizontal tanks, a small aspect ratio results in less boil-off and pressure increase in the storage tank over time. However, there are many other considerations that needs to be taken into account when optimizing for liquid hydrogen storage. For instance, in aviation there are strict requirements pertaining to how a fuel tank is to be integrated, and a small aspect ratio might not be the most desirable from both a practical and operational standpoint. Due to hydrogen being so light, the mass of the storage tank also becomes particularly important as it will make up the majority of the total weight. Hence, gravimetric efficiency — the mass of hydrogen stored inside the tank over the total mass – is an important indicator of the quality of the storage design. Figure 4.23 shows that the gravimetric efficiency of the lowest aspect ratio tank is worse than the other tanks, where AR 1 actually has the highest efficiency. When compared to Figure 4.22 it seems that this property is proportional to the total heat ingress into

the storage tank. This might not be a general trend, but it is a good example of how optimizing one design aspect can be a detriment to another. It should be stated that neither of the three tank proportions are particularly impressive in terms of gravimetric efficiency.

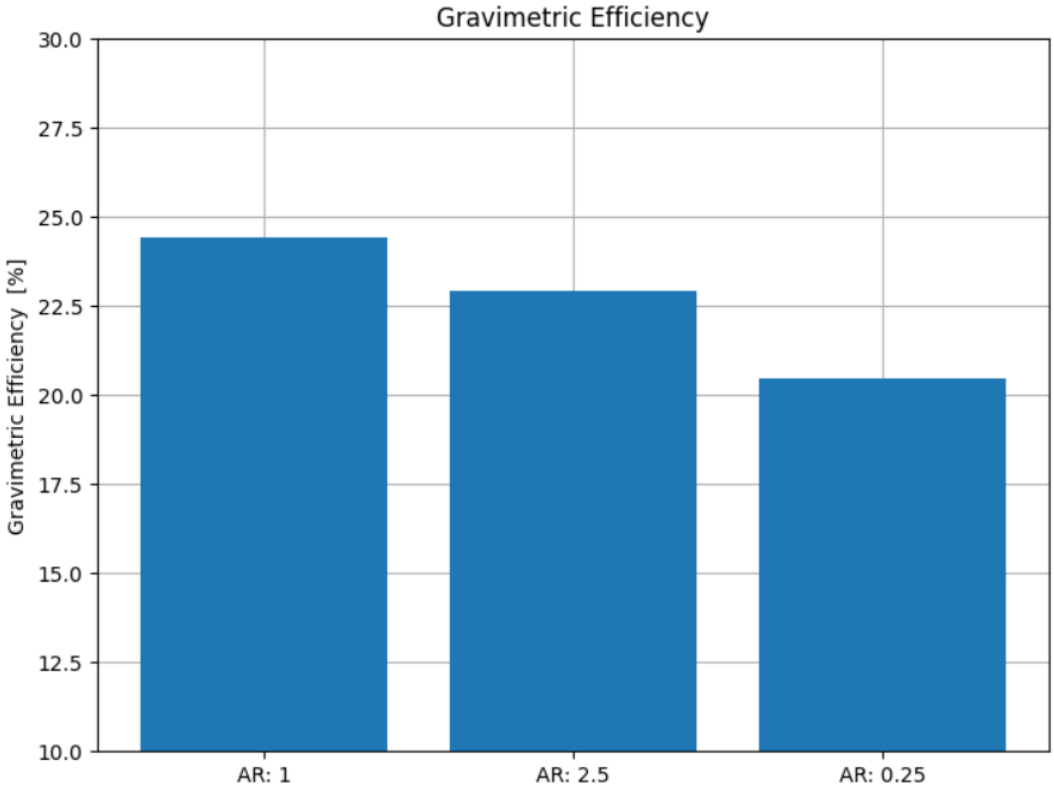

Figure 4.23 – Bar chart showing the gravimetric efficiency of each tank. The trend is the same as the one seen in Figure 4.22 in terms of total heat transfer.

This study was not made with the intention of concluding that any one tank shape is more optimal than another, but rather as a way to show that the model is able to efficiently simulate different tank dynamics and generate much of the data necessary to conduct proper optimization studies.

4.3 General discussion

The model validation in Section 4.1 showed some promising results that the model has the potential to capture some of the underlying dynamics behind self-pressurisation inside a liquid hydrogen storage tank when calibrated parameters are

used. It is unfortunate that certain model assumptions, in particular the ones regarding heat transfer at the interface, seem to be slightly too simplified to accurately describe the complex phenomena happening at this part of the tank. Updating these assumptions to also include convective heat transfer could be worthwhile, as here only a scaling factor was considered. In spite of this, it is believed that introduction of a temperature gradient via spacial discretization close to the interface is one of the main factors why such a good fit to experimental data was possible in the first place; therefore it is recommended to continue evaluating and developing this contribution in future renditions of the model. It is unclear how much dividing the liquid domain into several control volumes actually contribute to describing the thermal stratification phenomena. Results from both the validation and some of the conducted simulations suggests that the temperature in both the liquid bulk and in the boundary layer are so close in value only moments after starting the simulation that they are effectively homogeneous in temperature. Further investigation into the nature of the liquid stratification effects needs to be conducted before drawing any definitive conclusions regarding there usefulness.

4.3.1 Model robustness

There were several other studies that would have been interesting to test, but had to be excluded from the analysis either because of time constraints or issues with the model. In its current stage, the model suffers from sever problems with robustness, and there are a lot of initial conditions and/or parameter combinations that lead to the model having numerical issues or straight up fails to converge. This is partly the reason why the horizontal tank geometry was utilized to such an extend when simulating the different study cases, since other geometries and/or orientations often had issues executing the simulation without complications. This is not necessarily because the implemented geometry package in it self introduces errors that lead to the overall model having robustness issues (although this possibility should not be excluded), but instead there could be something fundamentally flawed with the source code of the model.

One likely source of the problem is how the mass and energy balances connecting each liquid control volume utilize fluid properties obtained from the medium package. All fluid properties are derived from non-linear equations using the two state variables pressure and specific enthalpy, and when these share algebraic equations

amongst them that need to be solved simultaneously then the solver has to use iteration. Almost every time the model fails to converge, it is more often than not due to the solver being unable to iteratively determine the next state derivatives for specific enthalpy of the liquid ($h_{LB(L),i}$) that would lead to a solution for these non-linear sets of equations. Possible reasons for why this is the case are mere conjecture, however, it might have something to do with how the states in all control volumes tend to converge onto a single value. Having constantly fluctuation control volume sizes could also maybe introduce some unknown effect that snowballs into a convergence error. Whatever the reason may be, it needs to be pinpointed and addressed before the model can be considered usable in any commercial sense. One solution to the problem could be to simplify the model by using only one set of fluid property values shared amongst all liquid control volumes. This might not be an unreasonable assumption since many variables seem to be very close in value regardless. The ideal solution would of course be not having to resort to this assumption, as the utilization of different non-constant fluid properties in each control volume is a feature that makes the proposed model stand out among many other low-dimensional models.

It is quite unfortunate that the model is unable to produce certain results because of the reasons discussed. However, the fact that it is able to generate any results, and that these are not obviously unreasonable, still might make it worth continuation of its development.

5 Future Work

5.1 Model improvements and considerations

The developed model is far from perfect to say the least, and there is still a lot of work needed before it can be considered suitable for implementation into any of Modelons standard libraries. Some potential improvements and considerations that ought to be addressed are listed below:

- The current iteration of the model has significant issues with respect to robustness, and as such there are inherent limitations when it comes to what can and cannot be simulated. A partial overhaul of the source code by more experienced modeling engineers would be recommended to make the model more robust, provided that this is even possible.
- There are still a myriad of different tank geometries and orientations that would be of interest for future versions of the model. For example, if the model is ever to be used to simulate pressure evolution and temperature distribution inside a hydrogen fuel tank onboard an aircraft, then it should be compatible with more unconventional geometries. Additionally, it should be able to support dynamic changes to the tank's orientation during liftoff and landing.
- It it desired to make the model more compatible with other components already available in the Modelon standard libraries, something that in hindsight should have been part of the fundamental model architecture from the very beginning. Examples of this includes heat ports for the vapor and liquid domains to allow for direct heating and/or cooling of the fluid via connectors to other components. Another big one is implementation of a more sophisticated dynamic wall model that supports discretization, as was already briefly mentioned in Section 3.3.
- Revision of empirical correlations used to determine convective flow rate, boundary layer thickness, and most of the heat transfer correlations would be advisable to ensure that these are representative of the different geometric

considerations. The assumption that the different factors used for one geometry being valid for other geometries in e.g., the boundary layer thickness is probably not a very accurate one.

5.2 Fluid property considerations

Even if the current model uses fairly complex dynamical fluid properties dependent on the state of the system, these do not take into consideration that hydrogen can exist in one of two different spin isomers: parahydrogen and orthohydrogen. Parahydrogen is at a lower energy state, meaning that conversion between the two isomeres at non-equilibrium conditions is associated with either heat release or absorbance [39]. This naturally has an effect on the pressure evolution in the tank, so extending the model to account for this non-equilibrium would be desirable in a future version. In the medium package currently employed, only parahydrogen is considered. However, Modelon has tools available for creating modelica implementations of medium properties, and there are readily accessible databases containing all the relevant properties for for the two isomers [40].

5.3 Additions to already existing models

Since it is not quite clear weather or not dividing the liquid domain into multiple control volumes and estimating flow characteristics using empirical correlations actually contributes to the overall fidelity of the developed model, it might be worth considering taking certain features from this model and implement them into the old tank model already availed in the Modelon ThermoFluid library. This is mainly referring to the introduction of a temperature gradient close to and subsequent heat and mass transfer at the interface, since these features seem to result in desirable dynamics relating to self-pressurization, as discussed in Section 4. The old model uses an approach similar to the bulk evaporation and condensation implementation presented in Section 3.5 as its sole means of energy and heat transfer across the interface. This means that the liquid and/or vapor needs to be saturated in order for any boil-off/condensation to occur. Adding the temperature gradient could therefore potentially be a good compliment to the old model dynamics. Another benefit of doing this is that it would solve the crippling issues with robustness that

plagues the developed model, as the old model component has no such issues.

6 Conclusion

A low-dimensional model that is capable of predicting complex physical phenomena occurring during liquid hydrogen storage was developed. The model is flexible with regard to several common geometries found in practical applications of cryogenic storage, with multiple user-friendly option implementations for extra customization.

The developed model showed reasonable agreement to experimental data when calibrated parameters where employed, however, it is hard to draw definitive conclusions regarding the fidelity of the model. Several studies were conducted and showed that when the model is working properly it can be used to investigate many different storage conditions and considerations, while also producing large amounts of data for analysis.

Persistent issues with model robustness is a major drawback that needs to be addressed, and a lot of work is still required to make the model more efficient and generally applicable before it can be considered suitable for public use. Despite this it is likely still worth continuing development of the proposed model, or adapt some of its features as implementations to already existing ones.

References

[1] Jon Huete and Pericles Pilidis. “Parametric study on tank integration for hydrogen civil aviation propulsion”. In: *International Journal of Hydrogen Energy* 46.1 (2021), pp. 37049–37062.

[2] Saif Z Al Ghafri et al. “Modeling of Liquid Hydrogen Boil Off”. In: *Energies* 15.3 (2022), p. 1149.

[3] *Self-pressurization of a flightweight liquid hydrogen storage tank subjected to low heat flux*. Vol. 5805. Prepared for the 1991 ASME/AIChE National Heat Transfer Conference. Minneapolis, Minnesota, 1991.

[4] Sebastian Verhelst and Thomas Wallner. “Hydrogen-fueled internal combustion engines”. In: *Progress in Energy and Combustion Science* 35.6 (2009), pp. 490–527.

[5] Nazim Muradov. “Low to near-zero CO2 production of hydrogen from fossil fuels: Status and perspectives”. In: *International Journal of Hydrogen Energy* 42.20 (1027), pp. 14058–14088.

[6] Airbus. *How to store liquid hydrogen for zero-emission flight*. [Online; accessed 02-May-2023]. 2021. URL: https://www.airbus.com/en/newsroom/news/2021-12-how-to-store-liquid-hydrogen-for-zero-emission-flight.

[7] Yogesh M Kurle, Sujing Wang, and Qiang Xu. “Simulation study on boil-off gas minimization and recovery strategies at LNG exporting terminals”. In: *Applied Energy* 156.15 (2015), pp. 628–641.

[8] Karl Verfondern. *Safety Considerations on Liquid Hydrogen*. Jülich, Germany: Forschungszentrum Jülich GmbH Zentralbiblothek, 2008.

[9] C S Lin, N T Van Dresar, and M M Hasan. “Pressure Control Analysis of Cryogenic Storage Systems”. In: *Journal of Propulsion and Power* 20.3 (1991).

[10] Zhan Liu, YangZhong Li, and Guoqing Zhou. “Study on thermal stratification in liquid hydrogen tank under different gravity levels”. In: *International Journal of Hydrogen Energy* 43.1 (2018), pp. 9369–9378.

[11] Jeswin Joseph, Gagan Agrawal, and Deepak K Agarwal. “Effect of insulation thickness on pressure evolution and thermal stratification in a cryogenic tank”. In: *Applied Thermal Engineering* 111 (2017), pp. 1629–1639.

[12] Matthew J Daigle et al. “Temperature Stratification in a Cryogenic Fuel Tank”. In: *Journal of Thermophysics and Heat Transfer* 27.1 (2013), pp. 116–126.

[13] S Gursu et al. “Analysis and Optimization of Thermal Stratification”. In: *Journal of Energy Resources Technology* 115.3 (1993), p. 221.

[14] R W Arnett and R O Voth. *A computer program for the calculation of thermal stratification and self-pressurization in a liquid hydrogen tank*. Tech. rep. N-72-24362. Boulder, Colorado (USA): National Bureau of Standards, May 1972.

[15] G C Vliet et al. "Analysis and Optimization of Thermal Stratification". In: *Spacecraft* 1.6 (2012), p. 666.

[16] Walter Duval and Balasubramaniam Ramaswamy. *Convection Effects on Thermal Stratification Inside Enclosures due to Wall Heat Flux*. Tech. rep. AIAA 2008-821. Reno, Nevada (USA): 46th AIAA Aerospace Sciences Meeting and Exhibit, 2012.

[17] Mansu Seo and Sangkwon Jeong. "Analysis of self-pressurization phenomenon of cryogenic fluid storage tank with thermal diffusion model". In: *Cryogenics* 50.9 (2010), pp. 549–555.

[18] C M Yu, Aydemir N U, and Venart J E. "Transient free convection and thermal stratification in uniformly-heated partially-filled horizontal cylindrical and spherical vessels". In: *Journal of Thermal Science* 1 (1992), pp. 144–122.

[19] JingJie Ren et al. "Simulation on thermal stratification and de-stratification in liquefied gas tanks". In: *International Journal of Hydrogen Energy* 38.10 (2013), pp. 4017–4023.

[20] Sangeun Roh et al. "Numerical study of transient natural convection in a pressurized LNG storage tank". In: *Applied Thermal Engineering* 52.1 (2013), pp. 209–220.

[21] Modelon. *About Modelon*. 2023. URL: `https://modelon.com/company/`.

[22] Hubertus Tummescheit. "Design and Implementation of Object-Oriented Model Libraries using Modelica". PhD thesis. Lund, Sweden: Lund Institute of Technology, Aug. 2002.

[23] E R Eckert and Thomas W Jackson. *Analysis of turbulent-free boundary layer on flat plate*. Tech. rep. 2207. Lewis Flight Propulsion Laboratory Cleveland, Ohio: National Advisory Committee for Aeronautics, 1993.

[24] Hermann Schlichting. *Boundary Layer Theory*. USA: McGraw-Hill, 1979.

[25] Viatcheslav V Osipov et al. "Dynamical Model of Rocket Propellant Loading with Liquid Hydrogen". In: *Journal of Spacecraft and Rockets* 48.6 (2011), pp. 987–998.

[26] Viatcheslav V Osipov and Cyrill B Muraov. "Dynamic condensation blocking in cryogenic refueling". In: *Applied Physics Letters* 93 (2008), pp. 1–2.

[27] David Ingerman, Vladimir Druskin, and Leonid Knizhnerman. "Optimal Finite Difference Grids and Rational Approximations of the Square Root I. Elliptic Problems". In: *Communications on Pure and Applied Mathmatics* 42.8 (2000), pp. 1039–1066.

[28] D Landau L and E M Lifshitz. "Fluid Mechanics". In: Second. Pergamon Press, 1987. Chap. Thermal Conduction in Fluids, pp. 200–207.

[29] Suhas V Patankar. *Numerical Heat Transfer and Fluid Flow*. USA: Hemisphere Publishing Corporation, 1980.

[30] H K Versteeg and W Malalasekera. *Computational Fluid Dynamics: The Finite Volume Method*. England: Pearson Education Limited, 1995.

[31] Frank P Incropera et al. "Fundamentals of Heat and Mass transfer". In: Sixth. John Wiley Sons, Inc, 2007.

[32] Stuart W Churchill and Humbert H Chu. "Correlating equations for laminar and turbulent free convection from a vertical plate". In: *International Journal of Heat and Mass Transfer* 18.11 (1975), pp. 1323–1329.

[33] W H Besant. "Conic Sections Treated Geometrically". In: Ninth. George Bell and Sons, 2009. Chap. The Ellipse.

[34] Mark B Vallarino. "A note on the Accuracy of Ramanujan's Approximative Formula for the Perimeter of an Ellipse". In: *Journal of Inequalities in Pure and Applied Mathematics* 7.1 (2006).

[35] B A Younglove. "Thermodynamic properties of fluid". In: *Journal of Physical and Chemical Reference Data* 11.1 (1982).

[36] Modelon. *From Modelica Model to Simulation Model: Compiler and Solver Insight, Lecture 3.4*. 2022. URL: https://help.modelon.com/latest/training/Day3/From_ModelicaModel_To_SimulationModel_Compiler_and_Solver_insights/.

[37] Wikipedia. *Nelder–Mead method*. [Online; accessed 01-May-2023]. 2023. URL: https://en.wikipedia.org/wiki/Nelder%E2%80%93Mead_method.

[38] *Mylar polyester film: Physical-Thermal Properties*. 222367D. DuPont Teijin Films. June 2003.

[39] Olga A Boeva et al. "Low-temperature ortho–para hydrogen conversion catalyzed by gold nanoparticles: Particle size does not affect the rate". In: *International Journal of Hydrogen Energy* 42.36 (2017), pp. 22897–22902.

[40] Eric Lemmon, Marcia Huber, and Mark McLinden. *NIST Standard Reference Database 23: Reference Fluid Thermodynamic and Transport Properties-REFPROP, Version 9.1*. en. 2013-05-07 2013. URL: https://tsapps.nist.gov/publication/get_pdf.cfm?pub_id=912382.

A Appendix

A.1 Fluid property equations of state

Below are some of the equations of state used by the medium package to determine the fluid properties of parahydrogen by Younglove.

32-term modified Benedict Webb-Ruben equation of state for pressure:

$$\begin{aligned} p = \rho RT &+ \rho^2(G_1T + G_2T^{1/2} + G_3 + G_4/T + G_5/T^2) \\ &+ \rho^3(G_6T + G_7 + G_8/T + G_9/T^2) \\ &+ \rho^4(G_{10}T + G_{11} + G_{12}/T) + \rho^5(G_{13}) \\ &+ \rho^6(G_{14}/T + G_{15}/T^2) + \rho^7(G_{16}/T) \\ &+ \rho^8(G_{17}/T + G_{18}/T^2) + \rho^9(G_{19}/T^2) \\ &+ \rho^3(G_{20}/T^2 + G_{21}/T^3)e^{\gamma\rho^2} \\ &+ \rho^5(G_{22}/T^2 + G_{23}/T^4)e^{\gamma\rho^2} \\ &+ \rho^7(G_{24}/T^2 + G_{25}/T^3)e^{\gamma\rho^2} \\ &+ \rho^9(G_{26}/T^2 + G_{27}/T^4)e^{\gamma\rho^2} \\ &+ \rho^{11}(G_{28}/T^2 + G_{29}/T^3)e^{\gamma\rho^2} \\ &+ \rho^{13}(G_{30}/T^2 + G_{31}/T^3 + G_{32}/T^4)e^{\gamma\rho^2} \end{aligned} \tag{A.1}$$

where $\gamma = -1/\rho_c^2$ and ρ_c is the critical molar density. G_i are parameters fitted to experimental data.

Enthalpy:

$$H(T,\rho) = H^\circ(T^\circ) + \frac{p - \rho RT}{\rho} + \int_0^\rho \left\{ \frac{p}{\rho^2} - \frac{T}{\rho^2}\left(\frac{\partial p}{\partial T}\right)_\rho \right\}_T d\rho + \int_{298.15}^T C_p' dT \tag{A.2}$$

Internal energy:

$$E(T,\rho) = H(T,\rho) - \frac{p}{\rho} \tag{A.3}$$

Specific heat:

$$C_p(T,\rho) = C_V(T,\rho) + \left\{ \frac{T}{\rho^2} \left(\frac{\partial^2 p}{\partial T^2} \right)_\rho \Big/ \left(\frac{\partial^2 p}{\partial \rho^2} \right)_T \right\} \tag{A.4}$$

where:

$$C_V(T,\rho) = C_p' - R \int_0^\rho \left\{ \frac{T}{\rho^2} \left(\frac{\partial^2 p}{\partial T^2} \right)_\rho \right\}_T d\rho \tag{A.5}$$

A.2 Bulk evaporation and condensation

This section covers the implementation of bulk evaporation ad condensation contributions to the overall system introduces in Section 3.5.

A.2.1 Steam quality

Modelica code for implementation of steam quality (fraction of vapor in liquid):

```
x_vap = noEvent(if p/p_crit < 1.0
then max(0.0, min(1.0, (hv - hL_sat)/max(hv_sat - hL_sat,
1e-6))) else 1.0) "Steam quality in the vapor volume";

for i in 1:n loop
    x_LB[i] = noEvent(if p/p_crit < 1.0
    then max(0.0, min(1.0, (hLB[i] - hL_sat)/max(hv_sat - hL_sat,
    1e-6))) else 1.0) "Steam quality in the liquid bulk volume";
    x_LL[i] = noEvent(if p/p_crit < 1.0
    then max(0.0, min(1.0, (hLL[i] - hL_sat)/max(hv_sat - hL_sat,
    1e-6))) else 1.0) "Steam quality in the liquid boundary layer
 volume";
end for;
```

A.2.2 Mass and energy balances

New liquid mass and energy balances:

$$\begin{aligned} \frac{d(m_{LB,i})}{dt} &= J_{LB,i+1} - J_{LB,i} - J_{LBL,i} - J_{LB,i}^{evap} \\ \frac{d(m_{LL,i})}{dt} &= J_{LL,i-1} - J_{LL,i} + J_{LBL,i} - J_{LL,i}^{evap} \end{aligned} \tag{A.6}$$

$$\begin{aligned} \frac{dU_{LB,i}}{dt} &= J_{LB,i+1}h_{LB,i+1} - J_{LB,i}h_{LB,i} - J_{LBL,i}h_{LBL,i} + \dot{W}_{LB,i} - h_{LB,i}\frac{dm_{LB,i}}{dt} - J_{LB,i}^{evap}h_{vap}^{sat} \\ \frac{dU_{LL,i}}{dt} &= \dot{Q}_{WL,i} + J_{LL,i-1}h_{LL,i-1} - J_{LL,i}h_{LL,i} + J_{LBL,i}h_{LBL,i} + \dot{W}_{LL,i} - h_{LL,i}\frac{dm_{LL,i}}{dt} - J_{LL,i}^{evap}h_{vap}^{sat} \end{aligned} \tag{A.7}$$

New vapor mass and energy balances:

$$\begin{aligned} \frac{d(m_V)}{dt} &= -(J_{cond} + J_{vent}) + \sum_{i=1}^{n} J_{LB,i}^{evap} + \sum_{i=2}^{n-1} J_{LL,i}^{evap} - J_v^{cond} \\ \frac{d(U_V)}{dt} &= \dot{Q}_{WV} - \dot{Q}_{VS} + \dot{W}_V - h_V\frac{dm_V}{dt} + \sum_{i=1}^{n} J_{LB,i}^{evap}h_{vap}^{sat} + \sum_{i=2}^{n-1} J_{LL,i}^{evap}h_{vap}^{sat} - J_v^{cond}h_{liq}^{sat} \end{aligned} \tag{A.8}$$